

NEUROSCIENCE

Oxygen imaging of hypoxic pockets in the mouse cerebral cortex

Felix R. M. Beinlich^{1*†}, Antonios Asiminas^{1†}, Verena Untiet¹, Zuzanna Bojarowska¹, Virginia Plá¹, Björn Sigurdsson¹, Vincenzo Timmel², Lukas Gehrig², Michael H. Graber², Hajime Hirase^{1,3}, Maiken Nedergaard^{1,3*}

Consciousness is lost within seconds upon cessation of cerebral blood flow. The brain cannot store oxygen, and interruption of oxidative phosphorylation is fatal within minutes. Yet only rudimentary knowledge exists regarding cortical partial oxygen tension (P_{O_2}) dynamics under physiological conditions. Here we introduce Green enhanced Nano-lantern (GeNL), a genetically encoded bioluminescent oxygen indicator for P_{O_2} imaging. In awake behaving mice, we uncover the existence of spontaneous, spatially defined “hypoxic pockets” and demonstrate their linkage to the abrogation of local capillary flow. Exercise reduced the burden of hypoxic pockets by 52% compared with rest. The study provides insight into cortical oxygen dynamics in awake behaving animals and concurrently establishes a tool to delineate the importance of oxygen tension in physiological processes and neurological diseases.

The human brain uses ~20% of total body oxygen consumption at rest (1–3). Delivery and demand of oxygen (O_2) are so finely balanced that maintaining tissue oxygenation may be the most critical of all brain functions. Yet our understanding of the dynamics of brain tissue oxygen tension (P_{O_2}) under physiological conditions remains limited, largely because of the lack of spatially precise measurement techniques for P_{O_2} imaging. Currently, tissue P_{O_2} can be measured by phosphorescence and by Clark-type electrodes (4, 5). Neither approach provides sufficiently high spatiotemporal sensitivity to detect physiological changes in cortical P_{O_2} .

We developed a methodology to measure relative changes in P_{O_2} using the oxygen-dependent reaction of a luminescent substrate guided by its enzyme expressed in astrocytes. This method has a superior signal-to-noise ratio due to its bioluminescence origin and a spatiotemporal resolution that can visualize the dynamics of cortical P_{O_2} in awake behaving mice. Green enhanced Nano-lantern (GeNL) is a luminescent fusion protein consisting of the luciferase NanoLuc (6) and the fluorescent protein mNeonGreen (7). During the enzymatic conversion of its luminescent substrate furimazine to furimamide, energy is emitted in the form of light (6). The fluorescent fusion protein acts as a fluorescence amplifier, increasing the quantum yield through Förster resonance energy transfer (FRET). The enzymatic reac-

tion of GeNL with furimazine depends on O_2 (Fig. 1A), and the intensity of the bioluminescence signal is linearly correlated to the availability of O_2 when O_2 is the rate-limiting factor in the enzymatic reaction (8).

Green enhanced Nano-lantern can detect oxygen in mouse cortex

To assess whether the oxygen dependency can be used in vivo to visualize spontaneous P_{O_2} dynamics in the brain, we expressed GeNL in cortical astrocytes of wild-type mice (fig. S1A) and measured bioluminescence intensity (BLI) after topical administration of the substrate furimazine through a cranial window (Fig. 1, A and B, and fig. S2). BLI followed cerebral P_{O_2} when O_2 concentration of the breathing air was changed stepwise from 10% to 40% under ketamine-xylazine (KX) anesthesia. The baseline level of air O_2 was kept at 20% and then changed for 1-min periods followed by a 1-min recovery phase at baseline levels (Fig. 1C). Changing the O_2 concentration from 20% to 40% increased BLI by ~200%, whereas a reduction of O_2 concentration in the inhaled air to 10% decreased BLI by ~50% from baseline (Fig. 1, D and E; fig. S3A; and movie S1). To record the absolute P_{O_2} in the BLI imaging field, we placed an O_2 -sensitive Clark-type microelectrode in the field of view during the calibration protocol (Fig. 1B). Cerebral P_{O_2} increased by 20 mmHg at 30% O_2 and by 50 mmHg at 40% O_2 and reduced by 10 mmHg from baseline at 10% O_2 (Fig. 1, D and E, and fig. S3A). The reaction time and slope of BLI occurred in parallel with the electrode recordings, indicating similar reaction times with no time lag between change in O_2 and change in BLI (fig. S3, B and C). BLI peaked faster than electrode recordings upon increase of O_2 concentration but declined at a similar rate when O_2 was lowered, perhaps indicating substrate availability limitations under conditions with unphysiologically high O_2 con-

centrations (fig. S3D). Δ BLI is correlated with ΔP_{O_2} in a linear manner (Fig. 1F), although the availability of free O_2 might limit the sensitivity at low O_2 supply. GeNL BLI is thus an accurate measure of relative P_{O_2} .

Increased metabolism leads to increased carbon dioxide (CO_2) concentrations as a by-product of cellular respiration. CO_2 is a known vasodilator and alters pH (9, 10). We thus investigated the pH change in brain tissue upon O_2 calibration to exclude the possibility of pH alterations causing the effect on BLI described above. Mice expressing the genetically encoded fluorescent pH sensor pHuji (11) in the extracellular space were implanted with a fiber photometry probe and exposed to the same protocol for O_2 calibration under KX anesthesia. Manipulating O_2 did not alter pH during O_2 calibration (fig. S4).

Activation of the whisker barrel cortex by contralateral whisker stimulation leads to an increase in local blood flow and an increase in P_{O_2} . We next imaged the whisker barrel cortex in awake behaving mice while stimulating the whiskers by air puffs to test whether BLI can detect the sensory-induced cortical P_{O_2} change. Mice were exposed to a series of 10 brief whisker stimulations (5 Hz, 50-ms duration for 10 s, 50-s interstimulation interval) (Fig. 1G) (12). During whisker stimulation, BLI increased in the field of view (Fig. 1H and movie S2), closely following the individual series of whisker stimulation trials (Fig. 1I). Moreover, KX-anesthetized mice with simultaneous O_2 microelectrode recording showed similar consistent correlation between BLI and ΔP_{O_2} (fig. S5). Notably, the amplitude and the timing of BLI response differed between awake and KX-anesthetized mice (fig. S6), supporting the notion that anesthesia dampens tissue P_{O_2} and functional hyperemia dynamics (13, 14).

Oxygen dynamics in the cerebral cortex

Continuous imaging of BLI showed that P_{O_2} under resting conditions was highly dynamic, exhibiting local transient dips in P_{O_2} (Fig. 2, A to C, and movie S3). These local hypoxic events were spatially constricted, lasting several seconds up to minutes, and typically showed a sharp on- and offset in relative tissue P_{O_2} (Fig. 2, C to E). Given their negative relative amplitude in P_{O_2} and the characteristic sharply defined border, we called these “hypoxic pockets.”

Hypoxic pockets were identified on the basis of their negative amplitude [$P_{O_2}(\Delta B/B)$], typical sharp on- and offset, clear edges, and long duration (fig. S7A and movie S4). Hypoxic pockets were observed throughout 20-min-long recordings (Fig. 2, F to H). In KX-anesthetized mice, 200 ± 22 hypoxic pockets (mean \pm SEM) were detected during this time (Fig. 2I). Within a single frame recorded at 1 Hz, 8.12 ± 0.04 hypoxic pockets were observed per square millimeter, covering $2.43 \pm 0.02\%$ of the field of view

¹Division of Glial Disease and Therapeutics, Center for Translational Neuromedicine, Faculty of Health and Medical Sciences, University of Copenhagen, 2200 Copenhagen, Denmark. ²School of Engineering, FHNW University of Applied Sciences and Arts Northwestern Switzerland, 5210 Windisch, Switzerland. ³Division of Glial Disease and Therapeutics, Center for Translational Neuromedicine, University of Rochester Medical Center, Rochester, NY 14642, USA. *Corresponding author. Email: felix.beinlich@sund.ku.dk (F.R.M.B.); nedergaard@urmc.rochester.edu (M.N.) †These authors contributed equally to this work.



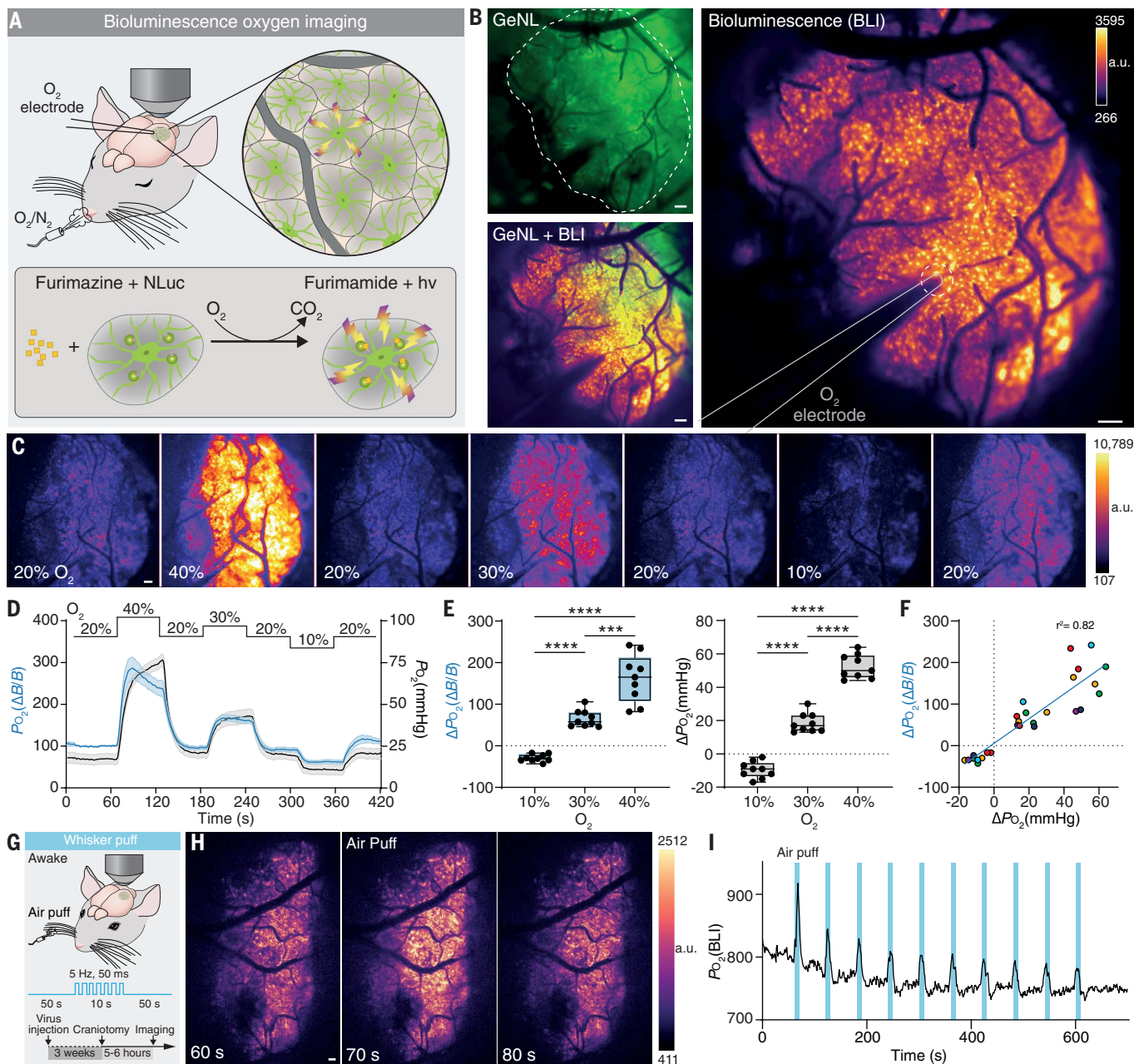


Fig. 1. Bioluminescence intensity of GeNL reports cerebral partial oxygen pressure. (A) (Top) Scheme of the experimental setup. KX-anesthetized mice expressing GeNL under glial fibrillary acidic protein promoter were placed under a microscope and exposed to different O_2 concentrations. An O_2 -sensitive microelectrode was inserted into the cortex through an acute craniotomy and artificial cerebrospinal fluid supplemented with furimazine (0.25 mM). (Bottom) Chemical reaction of furimazine to furimamide catalyzed by GeNL under presence of O_2 leading to light output in the form of bioluminescence. (B) Overlay of BLI and mNeonGreen fluorescence excited at 490 nm. Dashed line outlines the craniotomy; solid line outlines the oxygen-sensitive microelectrode. (C) BLI changes with varying concentrations of O_2 in the inhaled air. Single frames (1-s exposure time) at indicated O_2 concentrations throughout the calibration protocol. (D) Mean trace of the BLI and P_{O_2} as measured with the O_2 electrode at varying O_2 concentration. Shaded area indicates standard error. (E) BLI intensity [$P_{O_2}(\Delta B/B)$] changes 162% (± 19.13 , SEM) when O_2 concentration in the tidal air is doubled. A 10% increase in O_2 induces a 66% (± 6.70) increase. Under hypoxia, BLI is reduced by 29% (± 2.91). Accordingly, P_{O_2} increases by

52.4 mmHg (± 2.4) when O_2 concentration is doubled. A 10% increase in O_2 increases P_{O_2} by 18.6 mmHg (± 1.9), a 10% decrease reduces P_{O_2} by 9.7 mmHg (± 1.6). (Left) One-way repeated measures analysis of variance (ANOVA) $F_{1,272,10,18} = 82.66$, $P < 0.0001$ main effect of group. Tukey post hoc: 10% versus 30%, $P < 0.0001$; 10% versus 40%, $P < 0.0001$; 30% versus 40%, $P = 0.0006$. (Right) One-way repeated measures ANOVA $F_{1,523,12,18} = 219.7$, $P < 0.0001$ main effect of group. Tukey post hoc: 10% versus 30%, $P < 0.0001$; 10% versus 40%, $P < 0.0001$; 30% versus 40%, $P < 0.0001$. (F) Dependency of change in BLI and corresponding change in P_{O_2} recorded with the O_2 electrode in the same region upon changes in O_2 concentration of the inhalation air. Data points are fitted with a linear regression with a coefficient of determination, R^2 , of 0.82. Dots sharing the same color indicate data points from the same mouse. (G) Cerebral P_{O_2} was measured using BLI in somatosensory cortex of awake stationary head-fixed mice subjected to air-puff whisker stimulation. (H) Images from single frames at indicated time points before, during, and after a whisker puff. (I) Trace of ΔP_{O_2} upon whisker stimulation showing elevated P_{O_2} during each of the 10 repetitions. Means \pm SEM are shown. *** $P < 0.001$, **** $P < 0.0001$. [(D) to (F)] $N = 9$ trials from six mice. a.u., arbitrary units. Scale bars, 100 μm .

(Fig. 2, J and K). Hypoxic pockets covered an area of $1823 \pm 27 \mu\text{m}^2$ while lasting $48.2 \pm 1.0 \text{ s}$ (Fig. 2, L and M). $P_{\text{O}_2}(\Delta B/B)$ decreased by $27.2 \pm 4.5\%$ from baseline before each hypoxic pocket (Fig. 2N). Hypoxic pockets had an average diameter of $45.29 \pm 0.31 \mu\text{m}$ and an almost circular shape (Fig. 2, O and P). Hypoxic pockets often occurred repeatedly in the same area. Within a 20-min recording, on average 73.2 ± 5.1 of those regions of interest (ROIs) were detected with on average 2.8 ± 0.1 hypoxic pockets (Fig. 2, Q and R). Each minute, 0.15 ± 0.01 hypoxic pockets occurred within a given ROI, meaning that every $\sim 7 \text{ min}$, a hypoxic pocket occurred at the same place (Fig. 2S).

To quantify whether P_{O_2} during hypoxic pockets indeed reaches the hypoxic threshold

in the cortex ($\leq 18 \text{ mmHg}$) (15), we compared the $P_{\text{O}_2}(\Delta B/B)$ decrease in hypoxic pockets with those during hypoxia (10% inhaled O_2), where P_{O_2} reached 11 mmHg (Fig. 1D). During hypoxia, $P_{\text{O}_2}(\Delta B/B)$ was reduced by $29.2 \pm 2.9\%$, which is similar to the decrease observed in hypoxic pockets (fig. S8A). Using the electrode and BLI correlation, we determined that a 20.6% $\Delta B/B$ reduction corresponds to the hypoxic threshold (fig. S8B).

Spectral absorption by hemoglobin is a common cause of artifacts in imaging fluorescent biosensors in vivo (16). To exclude the possible signal interference by hemoglobin as the underlying cause of the hypoxic pockets, we recorded the mNeonGreen fluorescence of GeNL instead (fig. S9A). Hemoglobin absorption should also

affect the mNeonGreen fluorescence, which would be subject to hemoglobin absorption, but does not depend on O_2 . However, no events with similar spatiotemporal characteristics as hypoxic pockets were observed in the mNeonGreen fluorescence traces (fig. S9, B to E).

O_2 tension in and around venules is lower than in and around arterioles (17). We thus measured the distance of hypoxic pockets from arterioles and venules. Hypoxic pockets were closer to venules than to arterioles, with an average distance of 28.1 ± 0.7 and $48.0 \pm 1.2 \mu\text{m}$, respectively (fig. S10).

Tissue oxygenation is closely linked to the availability of O_2 and therefore to capillary circulation of red blood cells. We thus hypothesized that hypoxic pockets result from

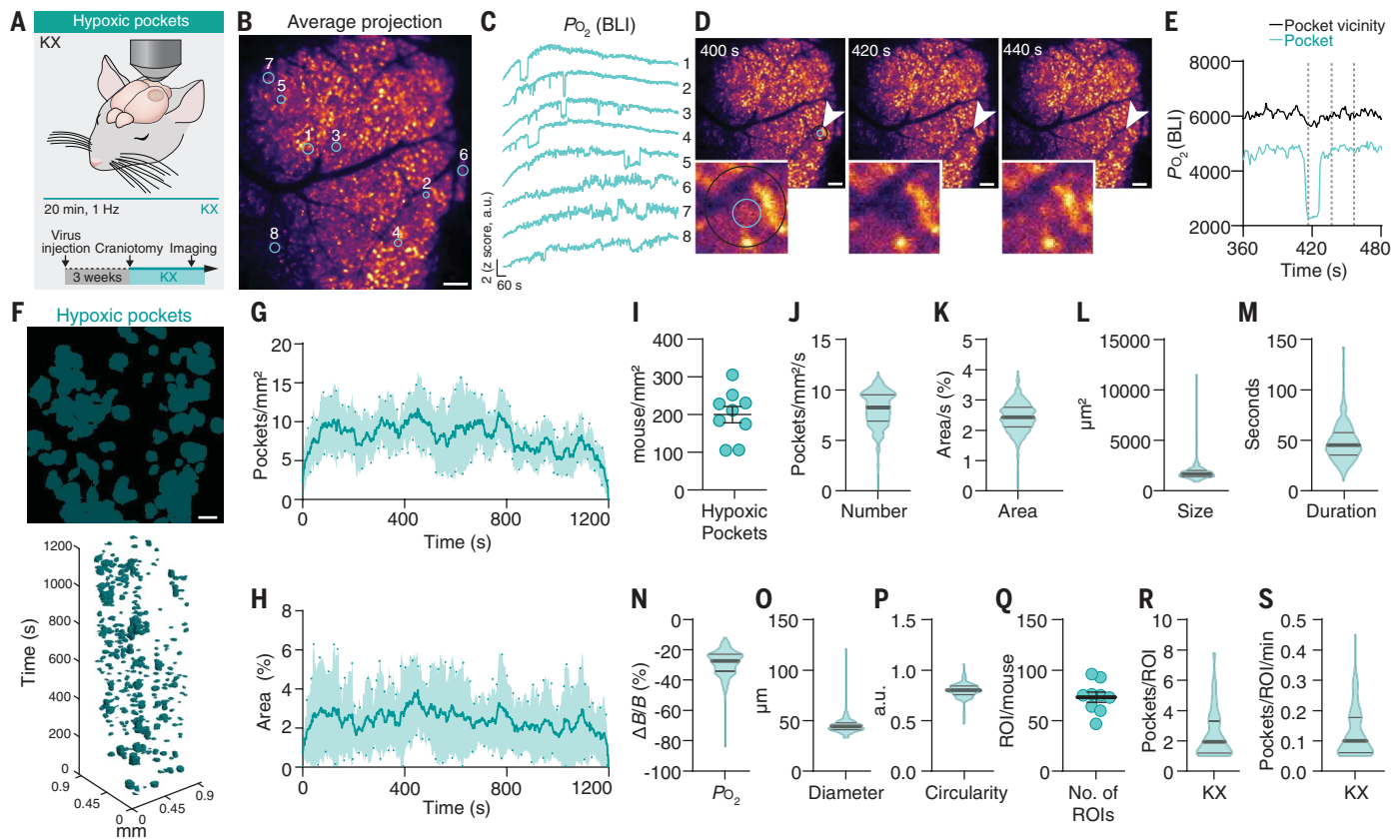


Fig. 2. Characterization of hypoxic pockets in cortex of anesthetized mice.

(A) Cerebral P_{O_2} was imaged in somatosensory cortex of KX-anesthetized mice over 20 min using BLI. (B) Average projection of BLI of the mouse cortex expressing GeNL in astrocytes after furimazine administration from a 20-min recording. (C) Time traces of the z-scored bioluminescent intensity of tissue P_{O_2} . Numbers indicate corresponding ROI from manually drawn circles in (B). (D) Images recorded at 400, 420, and 440 s from (B). Insets show magnification of the ROIs indicated by arrowheads [2 from (C)]. Inner circle defines area of pocket. The outer circle defines pocket vicinity. (E) Time trace of cerebral P_{O_2} from the ROI indicated by cyan (inner) and black (outer) circle in (D). (F) (Top) Average distribution of hypoxic pockets from (B). (Bottom) Hypoxic pockets during KX anesthesia in the form of ROIs over time displayed in an x - y - t 3D rendering. Cyan regions denote signal. (G) Line plot showing average number of hypoxic pockets per square millimeter per second over time. Shading indicates SEM. (H) Line plot showing average area of the field of view covered

by hypoxic pockets for each frame. Shading indicates SEM. (I) Average number of detected hypoxic pockets per square millimeter per mouse in a recording session. (J) Frequency distribution of number of hypoxic pockets per square millimeter per second. (K) Frequency distribution of area covered by hypoxic pockets per second. (L) Frequency distribution of size of hypoxic pockets. (M) Frequency distribution of duration of hypoxic pockets. (N) Frequency distribution of amplitude changes relative to baseline P_{O_2} of hypoxic pockets. (O) Frequency distribution of diameter of hypoxic pockets. (P) Frequency distribution of circularity of hypoxic pockets. (Q) Average number of active regions with reoccurring hypoxic pockets (ROIs) per mouse in a single recording session. (R) Frequency distribution of the number of hypoxic pockets for each detected active region. (S) Frequency distribution of the number of hypoxic pockets for each detected active region per minute. $N = 9$ mice (eight recorded for 20 min, one for 10 min). Violin plots show median and quartiles. Scale bars, $100 \mu\text{m}$.

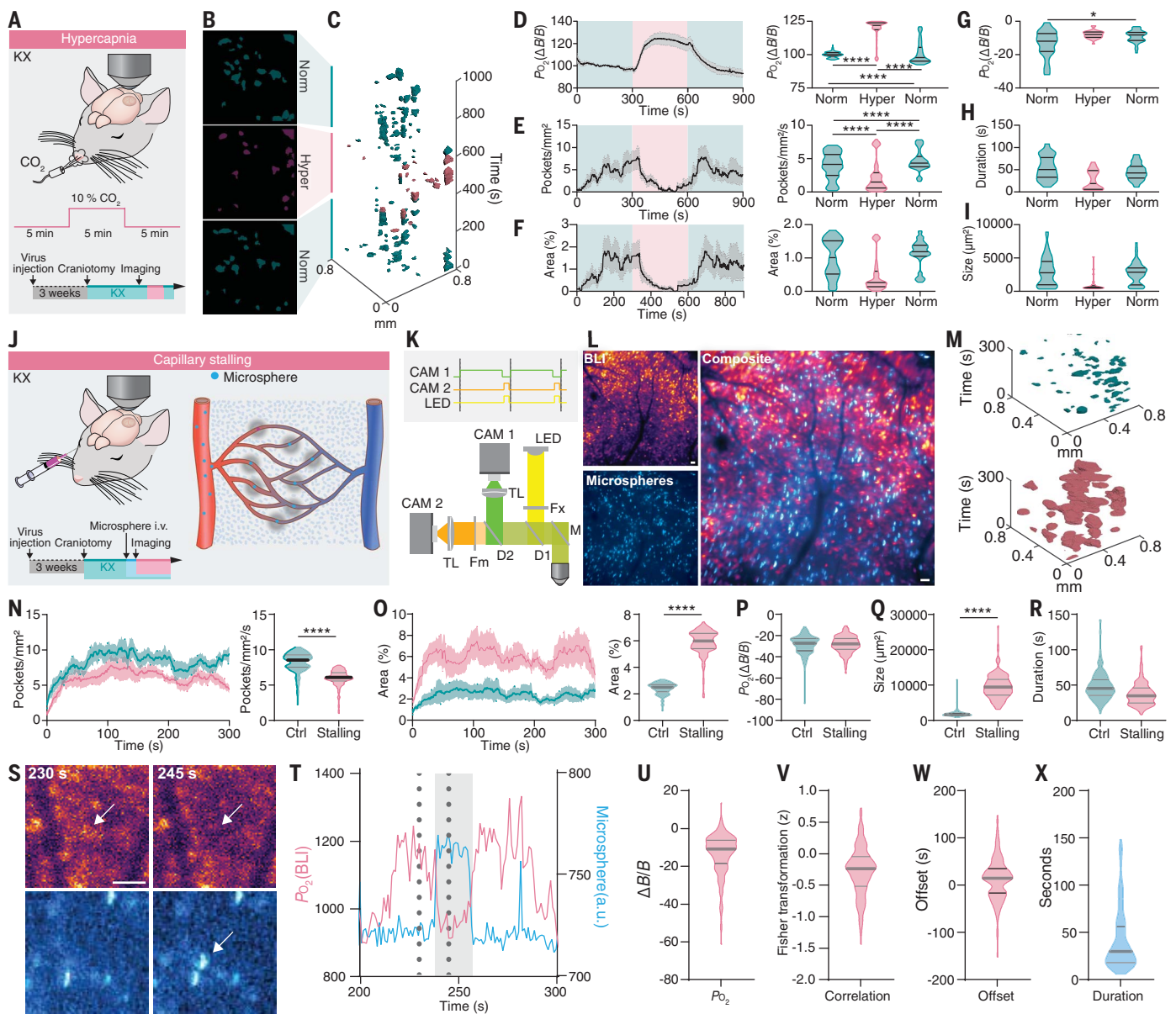


Fig. 3. Effects of vasodilation and capillary stalling on hypoxic pockets.

(A) Cerebral P_{O_2} was measured in KX-anesthetized mice exposed to 10% CO_2 in the inhaled air for 10 min after acute craniotomy. (B) Averages of the location of hypoxic pockets, before, during, and after hypercapnia. Norm, normocapnia; hyper, hypercapnia. (C) Hypoxic pockets during transition to and from hypercapnia, respectively, in the form of ROIs over time displayed in an x - y - t 3D rendering. Turquoise regions denote signal at normoxia, lilac regions denote signal during hypercapnia. (D) (Left) Average trace of cerebral P_{O_2} during the experiment. Lilac shading indicates the period of increased CO_2 , turquoise shading indicates periods of normal CO_2 levels. (Right) Frequency distribution of P_{O_2} per second in a 5-min window before, during, and after increased CO_2 . (E) (Left) Average trace of the number of hypoxic pockets per square millimeter. Lilac shading indicates period of increased CO_2 , turquoise shading indicates periods of normal CO_2 levels. (Right) Frequency distribution of number of pockets per square millimeter per second before, during, and after increased CO_2 . (F) (Left) Average trace of the area covered by hypoxic pockets. Lilac shading indicates period of increase CO_2 , turquoise shading indicates periods of normal CO_2 levels. (Right) Frequency distribution of area covered by hypoxic pockets per second in a 5-min window before, during, and after increased CO_2 . (G) Amplitude of hypoxic pockets before, during, and after CO_2 increase. (H) Duration of hypoxic pockets before,

during, and after CO_2 increase. (I) Size of hypoxic pockets before, during, and after CO_2 increase. (J) Cerebral P_{O_2} was measured with BLI in KX-anesthetized mice. Capillary stalling was induced by intravascular injection of 4- μ m microspheres before onset of imaging session. (K) The hybrid BLI-fluorescence microscope setup used to image BLI and microsphere fluorescence simultaneously. (L) (Left) Average intensity projection of BLI (top) and microsphere fluorescence (bottom). (Right) Overlay of BLI and microsphere fluorescence. (M) Hypoxic pockets in the form of ROIs over time displayed in an x - y - t 3D rendering. Turquoise regions denote signal under control, and lilac regions denote signal after injection of microspheres. (N) (Left) Average number of hypoxic pockets from control mice and after injection of microspheres. Shading indicates \pm SEM. (Right) Frequency distribution of number of hypoxic pockets per second in the cortex of control and microsphere-injected mice. (O) (Left) Average area covered by hypoxic pockets in control mice and mice injected with microspheres. Shading indicates \pm SEM. (Right) Frequency distribution of area covered by hypoxic pockets per second in the cortex of control and microsphere-injected mice. (P) Amplitude of hypoxic pockets. (Q) Size of hypoxic pockets. (R) Duration of hypoxic pockets. (S) Images recorded at 230 and 245 s from (L). Arrows indicate ROI. (T) Time trace of BLI (pink) and microsphere fluorescence (blue) from the ROI indicated by arrow in (S).

Dotted lines indicate time points of images in (S). Gray shading indicates time window where microsphere was visible. (U) Amplitude of BLI decrease during events where microspheres were stalled. (V) Fisher z-transformation of correlation coefficient of BLI and microsphere fluorescence. (W) Offset between BLI decrease normalized to microsphere onset. (X) Duration of

microsphere stalling. $N = 6$ mice, hypercapnia. $N = 9$ mice, control. $N = 5$ mice, microsphere injection. Means \pm SEM are shown. Violin plots show median and quartiles. Bars indicating Tukey's post hoc tests between groups at their edges: * $P < 0.05$, ** $P < 0.01$, *** $P < 0.001$, **** $P < 0.0001$. Scale bars, 100 μm .

hemodynamic changes in the microcirculation. We used intrinsic optical spectroscopy imaging (IOSI) (22, 26) to monitor hemoglobin dynamics in the brain of resting awake mice (fig. S11A). Hemoglobin dynamics were recorded at the isosbestic point for total hemoglobin concentration ([HbT]) (fig. S11B). The analysis identified areas of low [HbT] that shared their characteristic onset and offset dynamics with hypoxic pockets measured with BLI (fig. S9, C to F). On average 0.9 ± 0.01 events of low [HbT] were detected per square millimeter per second in IOSI measurements, which lasted 16.5 ± 0.4 s covering $7344 \pm 402 \mu\text{m}^2$ (fig. S11, G to J). During these events, [HbT] decreased by 1.9 ± 0.1 mmHg (fig. S11K). Whereas bioluminescence allows only the measurement of tissue hypoxia, IOSI reflects blood volume and thus transient localized decreases of hemoglobin concentration with similar temporal and spatial properties as shown for hypoxic pockets.

Effects of vasodilation and capillary stalling on hypoxic pockets

Brain activity is accompanied by transient increases in blood flow due to vasodilation, a phenomenon called neurovascular coupling or functional hyperemia (18). We asked whether hyperemia suppresses the number of hypoxic pockets and induces vasodilation by increasing CO_2 in air (hypercapnia) (Fig. 3A) (9). The elevation of CO_2 in the inhaled air increased tissue P_{O_2} reversibly to $118.4 \pm 0.3\%$ concurrently with a sharp decrease in the number of hypoxic pockets per square millimeter per second in a reversible manner, from 3.9 ± 0.1 to 2.3 ± 0.1 and back to 4.7 ± 0.1 , a reduction of 41% when CO_2 was lowered (Fig. 3, B to E). Area covered by hypoxic pockets changed by 0.54%, from $1.01 \pm 0.03\%$ to $0.47 \pm 0.02\%$, a reduction of 53% (Fig. 3F). $P_{\text{O}_2}(\Delta B/B)$ decrease within hypoxic pockets during hypercapnia was reduced by 4% and stayed low after hypercapnia during the time of recording (Fig. 3G). Furthermore, the duration of hypoxic pockets was reduced by 17 s, and their spatial expansion was reduced by 65% (Fig. 3, H and I). After resolution of hypercapnia, hypoxic pocket duration and size recovered (Fig. 3, H and I). This observation is consistent with the finding that hypercapnia decreases the portion of poorly perfused capillaries in the rat brain cortex (19). To assess whether an increased acidification during hypercapnia is involved (20), we measured extracellular pH in the brain parenchyma during 10% CO_2 as described above. A 5-min period of 10% CO_2 decreased pH_{uji} intensity by 6.4% in

a reversible manner (fig. S12). Typically, fluorescent proteins are quenched in acidic environments, yet we observed an increase in BLI during hypercapnia, excluding the possibility that the observation was an artificial effect of pH on the sensor's intensity.

Isoflurane is another potent vasodilator (21, 22) that increases blood volume but not tissue pH (23). We compared mice before and during isoflurane anesthesia and observed a decrease in the number of hypoxic pockets similar to that seen for CO_2 (fig. S13, A and B). During isoflurane anesthesia, the number of hypoxic pockets per second was effectively decreased from 6.2 ± 0.01 to 1.9 ± 0.03 , a reduction of 69% (fig. S13C). The area covered by hypoxic pockets was reduced by 0.83%, a decrease of 13% (fig. S13D). The $P_{\text{O}_2}(\Delta B/B)$ decrease within hypoxic pockets was 21% less in isoflurane-anesthetized mice than in awake mice, and duration decreased by 15 s (fig. S13, E and F). The size of hypoxic pockets was reduced by 13% (fig. S13G).

A direct consequence of hypercapnia and isoflurane anesthesia-induced vasodilation is an increase in tissue P_{O_2} (13, 24). Increased tissue P_{O_2} might compensate for low-oxygenated areas by increasing O_2 diffusion and thus reducing prevalence of hypoxic pockets (25). To uncouple vasodilation and tissue oxygenation, we increased the O_2 in the inhalation air from 20% to 30%, inducing hyperoxia (fig. S14, A to C). This led to a 55% increase in ΔP_{O_2} during hyperoxia, which is substantially higher than the increase measured under hypercapnia (fig. S14D). During hyperoxia, the number of hypoxic pockets per second dropped from 3.5 ± 0.04 to 3.1 ± 0.03 , a decrease of 11% (fig. S14E), which is far less compared with the isoflurane and hypercapnia conditions, where hypoxic pockets were reduced by 69 and 41%, respectively. During hyperoxia, $P_{\text{O}_2}(\Delta B/B)$ in hypoxic pockets decreased 15.9% less than during normoxia (fig. S14F), which might be explained by the accompanying increase in P_{O_2} leading to an overall increased tissue P_{O_2} , reducing the amplitude of the hypoxic pockets. Furthermore, the duration of hypoxic pockets was reduced by 13 s (41.5 ± 1 versus 28.5 ± 1 s), and their size increased slightly by 13% (fig. S14, G to H). These observations show that vasodilation more potently controls the hypoxic pockets than does blood oxygenation.

Local cerebral microcirculation is mainly regulated by changes of vascular resistance (26). Reversible adhesion of circulating leukocytes can effectively halt capillary blood flow, a phenomenon called capillary stalling (27). To directly test whether capillary stalling elicits hypoxic

pockets, microspheres (diameter: 4 μm) were delivered intravascularly (Fig. 3J) to occlude capillaries (28, 29). We recorded O_2 dynamics and microspheres in the same field of view simultaneously at 1 Hz using a hybrid BLI-fluorescence microscope that uses the readout time of the BLI camera to record microsphere fluorescence with a second camera (Fig. 3, K to M). After injection of microspheres, the number of hypoxic pockets decreased from 8.2 ± 0.07 to 5.9 ± 0.06 (Fig. 3N). In contrast, the total area covered by hypoxic pockets per second increased from 2.4% to 5.9%, an increase of 146% (Fig. 3O). Whereas $P_{\text{O}_2}(\Delta B/B)$ only marginally changed (Fig. 3P), the duration of microsphere-induced hypoxic pockets was 11 s shorter (Fig. 3R). Microsphere-induced hypoxic pockets were 445% larger than in the control group (Fig. 3Q). Taken together, upon microsphere injection, the area of hypoxic tissue was increased, as reflected by an increase in size but not in the number of pockets. A plausible explanation for this observation is that upon microsphere injection, hypoxic pockets near each other may have fused together, thus decreasing the number of individually detected events. When interrogating the dynamics of individual spheres and local tissue O_2 dynamics, it was clear that influx of a microsphere quickly triggered a local decrease in P_{O_2} with a similar temporal dynamic as the spontaneously occurring hypoxic pockets (Fig. 3, S to X).

Hypoxic pockets are reduced by wakefulness and further suppressed by locomotion

To detect O_2 dynamics in awake animals and assess the effect of locomotion, mice were trained to tolerate head restraint. One group of awake mice was recorded on a stationary platform, whereas a second group of mice was placed on a polystyrene ball allowing head-fixed locomotion (Fig. 4A). The number of hypoxic pockets in behaving mice was reduced by 17% compared to KX-anesthetized mice (Fig. 4, B, D, and F). Yet the pockets increased in surface area by 41% (Fig. 4J). Hypoxic pockets lasted on average 8 s less in awake mice, whereas the amplitude was unaffected (Fig. 4, H and I). Taken together, the P_{O_2} maintains the same characteristics but is more dynamic in the awake state than in the anesthetized state, possibly reflecting the higher level of neuronal activity and thereby blood flow in wakefulness compared with anesthesia (30, 31). We also sought to determine whether the number of hypoxic pockets correlates with mice actively running, where increased blood

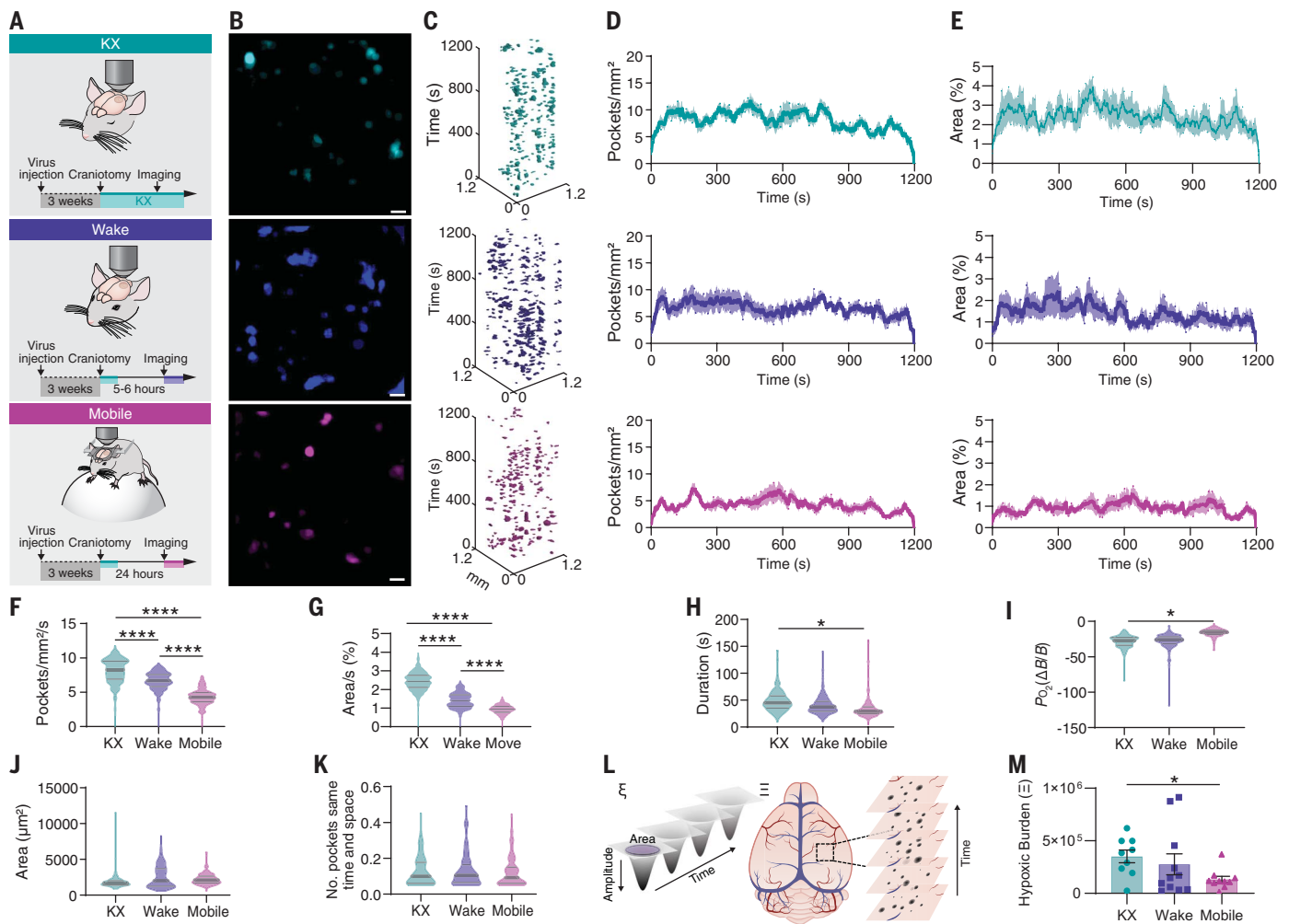


Fig. 4. Increased arousal level suppresses tissue hypoxia. (A) Cerebral P_{O_2} was either measured in KX-anesthetized mice, in awake head-fixed mice during quiet wakefulness in a MAG-1 mouse holder, or in mobile mice voluntarily running on a Styrofoam sphere. (B) Distribution of hypoxic pockets in a single recording session lasting 20 min. (C) Hypoxic pockets identified in (B) in the form of ROIs over time displayed in an x-y-t 3D rendering. Turquoise regions denote signal. (D) Average number of hypoxic pockets detected for each frame in mice during KX anesthesia, wakefulness, and mobile wakefulness, respectively. (E) Average area that hypoxic pockets cover in the field of view in percentage detected for each frame in mice during KX anesthesia, wakefulness, and mobile wakefulness, respectively. (F) Frequency distribution of number of hypoxic

pockets. (G) Frequency distribution of area covered by hypoxic pockets in the field of view per second. (H) Frequency distribution of duration of hypoxic pockets. (I) Frequency distribution of amplitude of hypoxic pockets. (J) Frequency distribution of size of hypoxic pockets. (K) Frequency distribution of number of hypoxic pockets sharing the same region per second. (L) Schematic illustrating the parameters used to calculate the hypoxic burden for each hypoxic pocket (left; ξ) and for an entire recording/mouse (right; Ξ). (M) Hypoxic burden during KX anesthesia, wakefulness, and mobile wakefulness. $N = 9$ mice, KX. $N = 11$ mice, awake. $N = 10$ mice, mobile. Means \pm SEM are shown. Violin plots show median and quartiles. Bars indicating Tukey's post hoc tests between groups at their edges: * $P < 0.05$, ** $P < 0.01$, *** $P < 0.001$, **** $P < 0.0001$. Scale bars, 100 μm .

flow and tissue P_{O_2} is expected (32). Twenty-four hours after surgery, mice were placed on an air-supported polystyrene ball (33), and P_{O_2} dynamics were recorded (Fig. 4, A to C). Compared with immobilized awake mice, the number of hypoxic pockets was reduced by 35%, from 6.7 ± 0.05 to 4.3 ± 0.03 , and the percentage of area covered by hypoxic pockets at any given time was reduced by 33% (Fig. 4, D to G). On average, hypoxic pockets lasted 7 s less in mice that could freely run (Fig. 4H). Further, the amplitude of hypoxic pockets was dampened by 10.4% compared with immobilized mice (Fig. 4I). The spatial coverage

of the hypoxic pockets was further reduced by 26% in running mice compared with immobile mice (Fig. 4J), whereas the number of ROIs of hypoxic pockets did not differ between KX-anesthetized, mobile, and immobile mice (Fig. 4K). It is unlikely that the decrease of hypoxic pockets during active locomotion is due to a general increase in blood flow, as their highly structured spatial characterization is preserved, which is in contrast to the expected general linear increase in blood flow. We summarized the burden of hypoxic pockets on the brain as a measure of the effect of area, duration, and amplitude (Fig. 4L). The analysis showed that the hypoxic

burden is reduced by 52% in running mice compared with quiet awake mice (Fig. 4M). Earlier studies have shown that sensory stimulation can reduce prevalence of capillary stalls (25). To test whether a similar paradigm suppresses the occurrence of hypoxic pockets, a series of 10 whisker stimulations were delivered to anesthetized mice (fig. S15A). The stimulation resulted in a 35% decrease in the number of hypoxic pockets (fig. S15, B to H). Thus, functional hyperemia suppressed the occurrence of hypoxic pockets, whether initiated by sensory stimulation in anesthetized mice or by active running in awake behaving mice (fig. S15, I to M).

Discussion

This study shows that relative changes in P_{O_2} can be monitored continuously in wide cortical regions of awake behaving mice by a genetically encoded bioluminescent oxygen indicator. By monitoring the bioluminescence signal of GeNL expressed in astrocytes, we found that cortical P_{O_2} constantly fluctuates during physiological conditions, giving rise to spatially and temporally defined hypoxic pockets. Manipulations that either increased or blocked capillary flow showed that local interruption of the microcirculation is responsible for the occurrence of hypoxic pockets. This conclusion was supported by imaging (i.e., IOSI) of cortical hemoglobin absorption. Monitoring of the local hemoglobin concentration identified transient local reduction in hemoglobin, which shared characteristic onset and offset dynamics with hypoxic pockets, thus providing an alternative approach to validate the occurrence of spatially restricted P_{O_2} fluctuations during physiological conditions.

Two-photon imaging of cortical capillaries has documented that the velocity of red blood cells can vary by more than a factor of 10 (34–36). A characteristic trait of the mammalian cortex is the unbalanced prevalence of arterioles and venules. A modeling study predicted that low-flow regions in the capillary bed are inevitable owing to the many sources and sinks of blood flow and that they tend to form around whichever vessel is more numerous (37). In contrast to humans, where the ratio is 2.5:1 (arterioles: venules), in mice, venules outnumber arterioles by a factor of 2.6 (38), which is expected to increase the low-flow regions preferentially around venules. Indeed, our analysis supported this notion by demonstrating that hypoxic pockets tend to appear closer to venules than to arterioles in mouse cortex.

We expressed GeNL under an astrocytic promoter to take advantage of the fact that the fine astrocytic processes infiltrate all parts of the neuropil (39, 40). However, we do not expect that the astrocyte-selective expression of GeNL had substantial impact on the observations. Oxygen diffuses freely across the neuropil with no restrictions imposed by either plasma membranes or by specific cell types (41, 42).

Why have hypoxic pockets not previously been detected? Recording P_{O_2} concentration with a temporal resolution of 225 to 400 s per frame found hypoxic micropockets in the cortex of awake old mice using the phosphorescence probe PtP-C343 (43, 44). However, the more frequent hypoxic events reported lasted only ~50 s and could not be detected when imaging with a slow, minute-lasting temporal resolution. Recently, 1/f-like fluctuations in P_{O_2} have been observed using Clark electrodes and linked to red blood cell spacing heterogeneity, in line with our observations (45). However, P_{O_2} declines with age (43, 46), and it would

be of interest to use the P_{O_2} bioluminescence imaging introduced here to assess whether aging is linked to progressive increase in the duration and/or spatial expansion of hypoxic pockets. Another open question is whether the transient hypoxic pockets contribute to the noise observed in the functional magnetic resonance imaging (fMRI) blood oxygen level-dependent (BOLD) signal. The hypoxic pockets are below the spatial resolution of fMRI but are likely contributing to the considerable noise during rest (47). It is in this regard that our analysis showed that the burden of the hypoxic pockets decreased when neuronal activity was increased, suggesting that the increase in BOLD signal may in part reflect a drop in occurrence of hypoxic pockets. This conclusion is supported by the finding that increase in capillary blood flow reduces the relative portion of capillary stalls (19).

Monitoring P_{O_2} with BLI is limited to detection of short-term fluctuations, excelling at measuring relative changes over periods of minutes rather than providing accurate baseline P_{O_2} comparisons over extended durations or across groups. It is important to note that although BLI is effective for assessing relative P_{O_2} , it does not offer absolute quantification.

Capillary blood flow is essential for supplying the brain with O_2 and glucose needed to support the high metabolic demand associated with normal brain function (48). Numerous studies have shown a link between reduced cerebral blood flow and cognitive decline (49–52), including changes in microvasculature structure and flow (29, 43). The existence of non-perfused capillaries were discovered decades ago (53). More recently, transient disruptions of flow, caused by neutrophil adhesion, at the single capillary level were identified as a potential mechanism that contributes to cerebral blood flow changes driving neurological deficits (54, 55). Increased capillary stalling has been observed in models of Alzheimer's disease (54), raising questions about the long-term impact of capillary stalling and its potential role in long-term neuronal viability. Hypoxia-induced increase in expression of hypoxia inducible factor 1 α (HIF1 α) impairs plasticity by disrupting synaptic physiology and spatial memory (56). Our study predicts that physical inactivity has direct effects on tissue P_{O_2} by favoring capillary occlusions and increasing the number of hypoxic pockets (fig. S16). Conversely, simply increasing sensory input or locomotion rapidly suppress the occurrence of hypoxic pockets, perhaps explaining the linkage between sedentary lifestyle and an increased risk of dementia (57, 58).

REFERENCES AND NOTES

1. S. S. Kety, in *Metabolism of the Nervous System*, D. Richter, Ed. (Pergamon, 1957), pp. 221–237.

2. D. D. Clarke, L. Sokoloff, in *Basic Neurochemistry: Molecular, Cellular and Medical Aspects*, G. J. Siegel, B. W. Agranoff, R. W. Albers, S. K. Fisher, M. D. Uhler, Eds. (Lippincott-Raven, ed. 6, 1999), pp. 637–689.
3. D. F. Rolfe, G. C. Brown, *Physiol. Rev.* **77**, 731–758 (1997).
4. T. Takano et al., *Nat. Neurosci.* **10**, 754–762 (2007).
5. B. Li et al., *eLife* **8**, e42299 (2019).
6. M. P. Hall et al., *ACS Chem. Biol.* **7**, 1848–1857 (2012).
7. K. Suzuki et al., *Nat. Commun.* **7**, 13718 (2016).
8. D. Lambrechts et al., *PLOS ONE* **9**, e97572 (2014).
9. R. A. Pollock, R. T. Jackson, A. A. Clairmont, W. L. Nicholson, *Arch. Otolaryngol.* **100**, 309–313 (1974).
10. J. Lee, T. Taira, P. Pihlaja, B. R. Ransom, K. Kaila, *Brain Res.* **706**, 210–216 (1996).
11. Y. Shen, M. Rosendale, R. E. Campbell, D. Perrais, *J. Cell Biol.* **207**, 419–432 (2014).
12. S. Holstein-Rønso et al., *Nat. Neurosci.* **26**, 1042–1053 (2023).
13. D. G. Lyons, A. Parpaleix, M. Roche, S. Charpak, *eLife* **5**, e12024 (2016).
14. A.-K. Aydin, C. Verdier, E. Chaigneau, S. Charpak, *Proc. Natl. Acad. Sci. U.S.A.* **119**, e2200205119 (2022).
15. K. Xu, D. A. Boas, S. Sakadžić, J. C. LaManna, *Adv. Exp. Med. Biol.* **977**, 149–153 (2017).
16. Y. Ma et al., *Proc. Natl. Acad. Sci. U.S.A.* **113**, E8463–E8471 (2016).
17. X. Zhu et al., *Light Sci. Appl.* **11**, 138 (2022).
18. A. R. Nippert, K. R. Biessecker, E. A. Newman, *Neuroscientist* **24**, 73–83 (2018).
19. A. Villringer, A. Thiem, U. Lindauer, K. Einhügel, U. Dirnagl, *Circ. Res.* **75**, 55–62 (1994).
20. D. A. Brodie, D. M. Woodbury, *Am. J. Physiol.* **192**, 91–94 (1958).
21. R. F. Cucchiara, R. A. Theye, J. D. Michenfelder, *Anesthesiology* **40**, 571–574 (1974).
22. S. Gelman, K. C. Fowler, L. R. Smith, *Anesth. Analg.* **63**, 557–565 (1984).
23. L. A. Low, L. C. Bauer, B. A. Klaunberg, *PLOS ONE* **11**, e0154936 (2016).
24. D. Aksenov, J. E. Eassa, J. Lakhoo, A. Wyrwicz, R. A. Linsenmeier, *Neurosci. Lett.* **524**, 116–118 (2012).
25. Ş. E. Erdener et al., *J. Cereb. Blood Flow Metab.* **39**, 886–900 (2019).
26. C. Iadecola, *Neuron* **96**, 17–42 (2017).
27. O. Bracko, J. C. Cruz Hernández, L. Park, N. Nishimura, C. B. Schaffer, *J. Cereb. Blood Flow Metab.* **41**, 1501–1516 (2021).
28. P. Reeson, B. Schager, M. Van Sprengel, C. E. Brown, *Front. Cell. Neurosci.* **16**, 876746 (2022).
29. P. Reeson, K. Choi, C. E. Brown, *eLife* **7**, e33670 (2018).
30. D. S. Greenberg, A. R. Houweling, J. N. D. Kerr, *Nat. Neurosci.* **11**, 749–751 (2008).
31. K. Masamoto, T. Obata, I. Kanno, *Adv. Exp. Med. Biol.* **662**, 57–61 (2010).
32. Q. Zhang et al., *Nat. Commun.* **10**, 5515 (2019).
33. V. Untiet et al., *Nat. Commun.* **14**, 1871 (2023).
34. E. Chaigneau, M. Oheim, E. Audinat, S. Charpak, *Proc. Natl. Acad. Sci. U.S.A.* **100**, 13081–13086 (2003).
35. H. S. Wei et al., *Neuron* **91**, 851–862 (2016).
36. J. Grutzendler, M. Nedergaard, *Trends Neurosci.* **42**, 528–536 (2019).
37. Y. Qi, M. Roper, *Proc. Natl. Acad. Sci. U.S.A.* **118**, e2021840118 (2021).
38. P. Blinder et al., *Nat. Neurosci.* **16**, 889–897 (2013).
39. K. Ogata, T. Kosaka, *Neuroscience* **113**, 221–233 (2002).
40. E. A. Bushong, M. E. Martone, Y. Z. Jones, M. H. Ellisman, *J. Neurosci.* **22**, 183–192 (2002).
41. K. A. Kasischke et al., *J. Cereb. Blood Flow Metab.* **31**, 68–81 (2011).
42. A. Krogh, *J. Physiol.* **52**, 409–415 (1919).
43. M. Moieni et al., *Sci. Rep.* **8**, 8219 (2018).
44. X. Lu et al., *Neurobiol. Aging* **88**, 11–23 (2020).
45. Q. Zhang, K. W. Gheres, P. J. Drew, *PLOS Biol.* **19**, e3001298 (2021).
46. C. Mathiesen, A. Brazhe, K. Thomsen, M. Lauritzen, *J. Cereb. Blood Flow Metab.* **33**, 161–169 (2013).
47. S.-G. Kim, S. Ogawa, *J. Cereb. Blood Flow Metab.* **32**, 1188–1206 (2012).
48. C. Iadecola, *Neuron* **80**, 844–866 (2013).
49. Y. Iturria-Medina et al., *Nat. Commun.* **7**, 11934 (2016).
50. J. C. de la Torre, *Stroke* **33**, 1152–1162 (2002).
51. R. N. Kalaria, *Neurobiol. Aging* **21**, 321–330 (2000).
52. E. Farkas, P. G. Luiten, *Prog. Neurobiol.* **64**, 575–611 (2001).
53. W. Kuschinsky, O. B. Paulson, *Cerebrovasc. Brain Metab. Rev.* **4**, 261–286 (1992).
54. J. C. Cruz Hernández et al., *Nat. Neurosci.* **22**, 413–420 (2019).
55. Ş. E. Erdener et al., *J. Cereb. Blood Flow Metab.* **41**, 236–252 (2021).

56. A. Arias-Cavieres *et al.*, *eNeuro* **7**, ENEURO.0024-20.2020 (2020).
57. S. Yan *et al.*, *Transl. Psychiatry* **10**, 112 (2020).
58. D. A. Raichlen *et al.*, *JAMA* **330**, 934–940 (2023).
59. F. R. M. Beinlich *et al.*, Oxygen Imaging of Hypoxic Pockets in the Mouse Cerebral Cortex [Data set], version 0.240215.0831, DANDI archive (2024); <https://doi.org/10.48324/dandi.000891/0.240215.0831>.
60. A. Asiminas, Temp2Spec/OxygenDynamics_Public: Science_2024, version Science_2024, Zenodo (2024); <https://doi.org/10.5281/zenodo.10629901>.

ACKNOWLEDGMENTS

We thank T. Nagai and S. Inagaki (Department of Biomolecular Science and Engineering, the Institute of Scientific and Industrial Research, Osaka University, Japan) for providing GeNL plasmid and helpful technical discussion. We also thank D. Xue for expert assistance with the illustrations, Y. Zhao for assistance with the data repository, and S. Goldman for comments on the manuscript. **Funding:** This work was supported by the Dr. Miriam and Sheldon G. Adelson Medical Research Foundation (M.N.); National Institutes of Health grant R01AT012312 (M.N.); NINDS R01AT011439 (M.N.);

U19 NS128613 (M.N.); the Simons Foundation (M.N.); Novo Nordisk Foundation NNF19OC0058058 (H.H.); Independent Research Fund Denmark 0134-00107B (H.H.); Novo Nordisk Foundation NNF20OC0066419 (M.N.); the Lundbeck Foundation R386-2021-165 (M.N.); JPND/HBCI 1098-00030B (M.N.); JPND/Good Vibes 2092-00006B (M.N.); DOD W911NF2110006 (M.N.); the Lundbeck Foundation R287-2018-2046 (V.U.); Independent Research Fund Denmark 0134-00107B (H.H.); Independent Research Fund Denmark 3101-00282B (M.N.); US Army Research Office grants MURI W911NF1910280 (M.N.); Marie Skłodowska-Curie Fellowship ANCoDy 101064009 (A.A.); and an ONO Rising Star Fellowship (A.A.). **Author contributions:** Conceptualization: F.R.M.B., H.H., and M.N. Methodology: F.R.M.B., A.A., V.U., Z.B., V.P., V.T., L.G., B.S., M.H.G., H.H., and M.N. Software: A.A., F.R.M.B., B.S., V.T., L.G., and M.H.G. Formal analysis: F.R.M.B., A.A., V.P., Z.B., V.T., L.G., M.H.G., and B.S. Investigation: F.R.M.B. and Z.B. Visualization: F.R.M.B. and A.A. Funding acquisition: H.H., M.N., V.U., and A.A. Project administration: F.R.M.B. and M.N. Supervision: F.R.M.B., M.H.G., H.H., and M.N. Writing – original draft: F.R.M.B., A.A., H.H., and M.N. Writing – review & editing: F.R.M.B., A.A., H.H., and M.N. **Competing interests:** The authors declare that they have no competing interests. **Data and materials availability:** The

microscope recordings are available at the DANDI archive (59). All data are available in the manuscript and the supplementary materials as data S1. Source code is deposited in Zenodo (60). **License information:** Copyright © 2024 the authors, some rights reserved; exclusive licensee American Association for the Advancement of Science. No claim to original US government works. <https://www.science.org/about/science-licenses-journal-article-reuse>

SUPPLEMENTARY MATERIALS

science.org/doi/10.1126/science.adn1011
Materials and Methods
Figs. S1 to S16
Tables S1 and S2
References (61–68)
MDAR Reproducibility Checklist
Movies S1 to S4
Data S1

Submitted 29 November 2023; accepted 23 February 2024
[10.1126/science.adn1011](https://doi.org/10.1126/science.adn1011)



Supplementary Materials for

Oxygen imaging of hypoxic pockets in the mouse cerebral cortex

Felix R. M. Beinlich *et al.*

Corresponding authors: Felix R. M. Beinlich, felix.beinlich@sund.ku.dk; Maiken Nedergaard, nedergaard@urmc.rochester.edu

Science **383**, 1471 (2024)
DOI: [10.1126/science.adn1011](https://doi.org/10.1126/science.adn1011)

The PDF file includes:

Materials and Methods
Figs. S1 to S16
Tables S1 and S2
References

Other Supplementary Material for this manuscript includes the following:

MDAR Reproducibility Checklist
Movies S1 to S4
Data S1

Materials and Methods

Animals and surgery

All experiments were conducted at the University of Copenhagen and were approved by the Danish Animal Experiments Inspectorate and overseen by the University of Copenhagen Institutional Animal Care and Use Committee (IACUC), in compliance with the European Communities Council Directive of 22 September 2010 (2010/63/EU) legislation governing the protection of animals used for scientific purposes (License number 2016-15-0201-01030 and 2020-15-0201-00483). C57BL/6JRj WT mice (Janvier) of both sexes were used in all experiments. Mice were housed in groups of 4 – 5 mice per cage in a temperature and humidity-controlled environment on a 12-hours light/dark cycle. They were fed with regular rodent chow and tap water ad libitum. Surgery was performed on 8 – 10 week old mice anesthetized with isoflurane (26675-46-7) (4 % induction, 1.5 % maintenance) or ketamine (6740-88-1)/xylazine (7361-61-7) (10 mg/ml and 1 mg/ml, respectively in 0.9 % saline, 0.1 ml/10 mg bodyweight i.p.). Body temperature was monitored throughout surgical procedures and maintained at 37°C. Data from animals presenting bleeding or a surgical injury were excluded from the analysis.

AAV injection

Virus injection was either performed locally into the brain using a stereotaxic frame or systemically via the i.v. route. Stereotaxic AAV injections were performed with a Hamilton syringe mounted to a micromanipulator (W.P.I.) at a 10-degree angle. At stereotaxic coordinates A/P: -1.97 mm, M/L: -3.0, V/D: -0.670 mm from bregma 700 nl virus at a concentration of 7×10^{12} vg/ml was injected at a rate of 100 nl/min. For i.v. injections 1×10^{11} vg were injected retro-orbitally in 0.9 % saline at a total volume of 100 μ l. All viruses used are listed in Table S1. Animals were imaged 2 – 4 weeks after injection and after a craniotomy was performed.

Chronic and acute craniotomies

A head plate was glued to the skull and a craniotomy was made above the right somatosensory cortex. Unless otherwise stated, after dura removal the window was covered with 1.3 % Agarose (Type III-A, High EEO, Sigma) supplemented with 5 % furimazine (Nano-Glo® Luciferase Assay, N1110, Promega). To prevent the agarose from drying out, the agarose was covered with aCSF (135 mM Na⁺, 142.8 mM Cl⁻, 4.2 mM K⁺, 1 mM Ca²⁺, 0.8 mM Mg²⁺, 10 mM Glucose, 10 mM HEPES) containing 5 % furimazine. On top of that, aCSF was sealed with a cover glass glued to the headplate with silicone (Kwick-Cast, W.P.I.). For recordings with the microelectrode the cover glass was not used. For chronic craniotomies, the window was sealed with a glass coverslip after dura removal.

In vivo oxygen calibration

For oxygen calibration of GeNL bioluminescence intensity, K/X anesthetized mice were used after acute craniotomy. Mice were fixed in a MAG-1 mouse holder (Narishige, Japan) and placed into a heat-insulation chamber (custom made, University of Copenhagen) with inlets for nosecone, exhaust tubing, and tubes for whisker stimulation via air puffs. Access to the craniotomy was

provided by a cut-out fitting the inner diameter of the head plate. The animal was provided with fresh air at defined O₂/N₂ ratio controlled by a gas mixer. The heat-insulation chamber was fitted under a microscope (Nikon AZ100M, Nikon). Expression of GeNL was verified by mNeonGreen fluorescence (490 nm LED, pE4000, CoolLED, FITC/Cy5 dual-band filter set F56-200, AHF Analysentechnik). BLI was recorded at 1 Hz with an EMCCD camera (Andor iXon 897 Ultra, Andor) via a 1x Objective (AZ Plan Apo 1x, NA 0.1, 35 mm WD). Camera settings were set to: 1s exposure time per frame, 512 x 512pixel, EM Gain 17 MHz at 16-bit, Conversion Gain 3x, EM Gain Multiplier 300x, temperature -72°C. The AZ100M was further equipped with an AZ-TE80 trinocular tube with a sliding 1-8x magnification and a 10/90 % filter to the EMCCD. Images were collected with NIS-Elements AR (Version 5.02.00, Nikon), stored as uncompressed tiff files, and post-processed with Fiji (59).

A Clark-type electrode microsensor (OX-10 fast, Unisense A/S, Aarhus, Denmark) with a 90 % response time of < 0.3 s and an outside tip diameter of 8 – 12 µm (60) was inserted ~ 50 – 100 µm into the cortex near the GeNL expression. Previously, the electrode was calibrated by two-point calibration in air-saturated 0.9 % saline and anoxic sodium ascorbate/sodium hydroxide (0.1 M). All microsensors were connected to a Microsensor Monometer (Unisense A/S) and data recorded with UniAmp (Unisense A/S). The beginnings of the recordings were marked with a trigger signal from the camera in the UniAmp software. A micromanipulator (MP-225, WPI) was used to control the position of the microsensor in the brain.

BLI recordings were normalized to the average BLI of the first 60 seconds at normoxic conditions. Intensity changes upon O₂ concentration change were calculated as the average of the last 30 seconds of each indicated O₂ level (e.g. 30 – 60 s for 20%, 90 – 120 s for 40%) where the signal was stable. Onset time was calculated as the time from changing O₂ concentration until signal increase or decrease from baseline by normalizing the signal to the maximum within the 60 second window of the manipulation duration. Peak time was calculated as the time between changing O₂ concentration until peak of the signal within the 60 seconds of manipulation has been reached.

Whisker stimulation

Neurons in the barrel-field cortex of the right hemisphere were stimulated 10 times by a series of air puffs (5 Hz, 50 ms, 20 psi) to contralateral whisker of the mouse over a time of 10 s with a break of 50 s between each trial or in periods of 90 s with 30 s stimulation time as described before (12, 33, 61). A custom developed Matlab routine was used to calculate the mean of the whisker puff stimulation trials for each animal.

In vivo bioluminescence imaging

In vivo bioluminescence imaging was performed on K/X anesthetized or awake head-fixed mice, immobilized in a MAG-1 mouse holder or voluntarily running on a Styrofoam sphere. A self-build microscope (Cerna, Thorlabs) equipped with either a 2x (TL2X-SAP, Thorlabs) or 4x (and RMS4X-PF, Olympus) objective was used. Bioluminescence was recorded with a cooled EMCCD camera (Andor iXon Ultra 897) at 1 Hz. Camera settings were set to: 1s exposure time per frame, 512 x 512pixel, EM Gain 17 MHz at 16-bit, Conversion Gain 3x, EM Gain Multiplier 300x, temperature -72°C. In some cases an Andor iXon Ultra 888 was used instead. GeNL expression was verified by mNeonGreen fluorescence. Briefly, mNeonGreen was excited using a 470 nm LED (CoolLED pE-4000) and filtered by a dual band filter set (59904, Chroma). Emitted light was

filtered with a 500 nm (ET500LP, Chroma) long pass filter for mNeogreen emission. In cases where mNeonGreen fluorescence was used to measure if local hemoglobin absorption reflects in negative changes in fluorescence similar those seen with BLI, mNeonGreen fluorescence was recorded at 1 Hz (Andor iXon 888 Ultra, bin2, Gain 2). Images were collected with μ Manager (Version 2.0) (62), stored as 16-bit uncompressed tiff files and post-processed with Fiji (59).

Intrinsic Optical Spectroscopy Imaging (IOSI)

IOSI was performed on awake head-fixed mice, immobilized in a MAG-1 mouse holder. Brain tissue was illuminated by collimated (525 nm, CoolLED pE-4000) and filtered (FF01-530/11, Semrock) light directly guided to the brain surface via a bifurcated fiber (BF19Y2HS02, Thorlabs). A 2x magnification objective was used for recordings (TL2X-SAP, Thorlabs). Reflected light was filtered by a 650 nm short pass filter (FESH 650, Thorlabs) to exclude infra-red light from the observation LED (850 nm, Thorlabs) and recorded at 1 Hz (960 ms exposure time, bin 2, Andor iXon Ultra 888, Andor) with μ Manager. Image files were stored as 16-bit uncompressed tiff files. The camera was triggered by a Master-8 pulse generator.

Microsphere injection and in vivo macroscopic imaging

Capillary stalling was induced by i.v. injection of 4 μ m microspheres (28). Red microspheres (4 μ m, 2% solids, FluoSpheres F8859, Invitrogen) were diluted (1:5) in saline and injected i.v. after sonication via retro-orbital injection before imaging under KX anesthesia as described above. Microspheres were recorded during bioluminescent oxygen imaging utilizing the readout phase of the BLI recording camera using a self-built two camera microscope. Briefly, red microspheres were excited by 550 nm LED (pE4000, CoolLED) filtered through a 488/561 dual color filter set (59904, Chroma) and guided to the animal via a 2x objective (TL2X-SAP, Thorlabs). Emitted fluorescence was collected with an EMCCD camera (Andor iXon 888 Ultra, Andor) after passing the 488/561 dual color filter set and a 543 nm dichroic mirror (ZT543-rdc-UF1, Chroma). In parallel BLI from the oxygen probe was collected via the same optical path but recorded with a second EMCCD camera (Andor iXon 897 Ultra, Andor). Both cameras and the LED were controlled by TTL pulses coming from a Master-8 pulse generator. Images were collected with μ Manager (Version 2.0) (62), stored as 16-bit uncompressed tiff files and post-processed with Fiji (59).

In vivo pH measurement

After virus injection using a 10 μ L glass Hamilton syringe (NF35BV-2, Nanofil, WPI) mounted to a Nanoinjector pump (Micro4, WPI), in the center of the injection site a mono fiber-optic cannula (400 μ m, 0.48 NA, Doric Lenses) attached to a 2.5 mm diameter metal ferrule was implanted. A concentration of 1.8×10^{13} vg/mL PHP.eB AAV2 GFAP-ILP.pHuji.PTD virus was injected at stereotaxic coordinates A/P: -1.7 mm, M/L: --3.0, V/D: -0.9, -1.0.X, -1.1.X mm from bregma. Animals were imaged 2 – 4 weeks after injection.

Fiber photometry

The pH sensitive fluorescent biosensor was excited by an LED (560 nm, Tucker Davis Technologies). Together with a second LED (405 nm, Tucker Davis Technologies) used to correct for motion artifacts both were connected to a minicube (SPECS, Doric Lenses) by attenuator patch cords (400- μm core, NA = 0.48, Doric Lenses). LEDs were controlled by LED drivers Tucker Davis Technologies) and connected to RZ10-X real-time processor (Tucker-Davis Technologies). Fiber optic patch cords (400 μm core, NA = 0.48, Doric Lenses) connected the minicubes with the animals and connected via Zirconia sleeves to attach the fiber optic patch cord to fiber implants on the animal. 560 nm/405 nm excitation were sinusoidally modulated at 531 Hz/210 Hz.

Synapse (Tucker-Davis Technologies) was used to control the signal processor and collect data. Files were exported for analysis to MATLAB (MathWorks) as described before (63). Mice were recorded und KX anesthesia when oxygen concentration of the inhaled air was changed. For pH measurements under Hypercapnia, mice were recorded awake.

The $\Delta F/F$ calculations relied on the fitting of the 405 nm signal. To achieve normalization, the 560 nm signal and the 405 channel underwent scaling using the least-squares method, specifically utilizing the MATLAB first degree *polyfit()* function. This process determined the slope and intercept required to produce a scaled 405 nm channel. $\Delta F/F$ was obtained by subtracting the fitted control channel from the signal channel and dividing it by fitted controlled channel. Subsequently, $\Delta F/F$ was filtered with zero-phase digital filter to remove noise and down sampled by a factor of 100.

Immunohistochemistry

Mice were transcardially perfused with 20 mL 0.01 M phosphate buffered saline (PBS, pH 7.4, Sigma-Aldrich) and 20 mL of 4% paraformaldehyde solution (PFA, Sigma-Aldrich) diluted in PBS pH 7.4 under deep K/X anesthesia. The brain was harvested and post-fixed in 4% PFA overnight and sliced in 100 μm -thick coronal sections using a vibratome (VT1200S, Leica). Then, free floating immunolabelling was performed to identify the cell identity of the viral-construct infected cells. Brain sections were incubated for 1 h at room temperature in 10% normal donkey serum-PBS containing 0.1% Triton X-100 and 0.2% gelatin and 40 $\mu\text{g}/\text{mL}$ AffiniPure Fab Fragment Donkey Anti-Mouse (715-007-003, Jackson Immunoresearch, UK) to suppress nonspecific binding. Primary antibodies were incubated overnight at 4C in PBS containing 5% normal donkey serum, 0.1% Triton X-100 and 0.2% gelatin followed by 3, 5-min washes in PBS. Secondary antibodies were incubated for 2 h at room temperature (1:500; Jackson ImmunoResearch; catalog 711175152 and 705175147). The specificity of the immunostaining was tested by omitting the primary antibodies (data not shown). Multichannel Z-stacks (20 μm , 1 μm step size) were acquired using the same acquisition parameters for all samples using a confocal microscope (Nikon Eclipse Ti, Tokyo, Japan).

Processing and analysis of BLI recordings

Macroscopic recordings were corrected for motion errors with the motion correction plugin of EZcalcium (64) and post-processed in Fiji (59). In addition to full field of view analysis, manually defined, rectangular (Fig. S5) or circular (Fig 2B) regions of interest were selected in the field of view and their mean traces over time were inspected.

Hypoxic Pocket detection. Hypoxic pockets were detected with custom developed Matlab routines (available at: <https://doi.org/10.5281/zenodo.10629901>). Briefly, after motion correction raw image files were first detrended on a pixel-by-pixel basis using a 3rd degree polynomial fit to correct for bioluminescence intensity reduction over time caused by substrate concentration decrease. To account for variability in the field of view across animals we defined the active recording tissue area. All pixels with values above the entire frame mean for at least 25% of the recording duration were defined as part of the active recording tissue area. Isolated pixels enclosed in the active recording area were also defined as part of it. The size of active recording tissue in mm² was used to normalize hypoxic pocket events in order to be able to compare across subjects. The detrended images were z-scored. Time traces for each pixel were z scored using following formula:

$$z = \frac{x-\mu}{\sigma} \text{ (Eq. 1)}$$

where x is the raw trace over time, μ is the mean value across time, and σ is the standard deviation of the signal over time.

The z-scored image was further filtered with a mean spatial filter with 21x21 pixel moving window. Hypoxic pockets were identified first on each frame of the smoothed imaging data, as areas with inverted signal above the 98% percentile that were part of the active recording tissue area. Based on our observations and given the absence of an existing analysis methodology, we excluded areas with less than 100 and more than 6400 pixels, and with less than 0.3 circularity score, calculated with function Matlab *regionprops()*, as:

$$\text{circularity} = \left(\frac{4*\pi*Area}{Perimeter^2} \right) * \left(1 - \frac{0.5}{r} \right)^2 \text{ (Eq. 2)}$$

where *perimeter* and *Area* are the distance around the boundary of the region in pixels and number of pixels in the region respectively, and r is defined as:

$$r = \frac{Perimeter}{2*\pi} + 0.5 \text{ (Eq. 3)}$$

The maximum circularity value is 1 for a circle and 0 for highly irregular areas.

Hypoxic pockets were tracked across frames based on their spatial overlap and subsequently filtered based on empirically set duration thresholds (3 s < < 150 s). Areas in the field of view found to produce hypoxic pocket events were termed regions of interest (ROIs) (see Fig 2Q-S). The mean detrended signal was extracted for each of these ROIs from the detrended image by summing pixel values for each frame, and their statistics such as area, diameter, perimeter, circularity, centroid coordinates, and signal change for individual hypoxic events they produced were calculated and correlated with other experimental parameters (e.g. movement, level of anesthesia etc.). Specifically for signal change, referred to as amplitude or $pO_2(\Delta B/B)$ in the manuscript/figures, this was calculated as signal change relative to the signal for 20 s before the hypoxic pocket event. For hypoxic events that took place within the first 20 s of recording baseline was taken as the 20 s after the end the event. To be able to compare the number of hypoxic pockets over time between different recordings/animals, the number of hypoxic pockets was normalized to a recording area of 1 mm² to correct for the different objectives and magnifications used. Briefly, a correction factor (κ) for each recording was determined:

$$\kappa = \frac{1000}{FOV \text{ edge}} \text{ (Eq. 4)}$$

Where *FOV edge* is the length in μm of the square field of view of any given recording area.

Hypoxic burden. We calculated the hypoxic burden (Ξ) for each recording as a measure for the influence of hypoxic pocket parameters on tissue $p\text{O}_2$. First, the hypoxic burden for an individual hypoxic pocket (ξ) was defined as:

$$\xi = \textit{duration} * \textit{amplitude} * \textit{area} \text{ (Eq. 5)}$$

Where *duration* in seconds, amplitude ($p\text{O}_2(\Delta\text{B}/\text{B})$) as positive signal change from baseline expressed as a fraction (e.g. 27% signal decrease during a hypoxic pocket = 0.27), and area in μm^2 . Next, the hypoxic burden (Ξ) of a single mouse during a recording was calculated as the sum of ξ for all (n) pockets of each recording, multiplied by the correction factor (κ) to account for FOV differences, and normalized to the length of recording in minutes:

$$\Xi = \sum_{i=1}^n \xi_i * \kappa / T_{rec} \text{ (Eq. 6)}$$

With T_{rec} being the recording length in minute.

IOS analysis

To identify changes in IOS imaging that could resemble spatiotemporal characteristic of hypoxic pockets, the raw recordings were first inverted to account for the inverted nature of the raw IOSI signal and normalized ($\Delta\text{R}/\text{R}$). The inverted $\Delta\text{R}/\text{R}$ image stack was then analyzed for the occurrence of hypoxic pockets with the algorithm as described above.

Hemoglobin changes within the identified hypoxic pockets was calculated as follows: We first estimated the weighted Beers-Lambert law coefficients using previously published method by Turner et al. (65). We used these coefficients to calculate hemoglobin concentrations and convert raw IOS imaging data. Using the masks created earlier during hypoxic pocket event identification. The relative change in hemoglobin concentration during events identified earlier was calculated by averaging the hemoglobin-estimation signal across all pixels of each event area and calculating the difference in total hemoglobin during the event duration relatively to a period of 20 s before, as previously described for BLI data.

Statistics and reproducibility

No statistical methods were used to pre-determine sample sizes. For statistical comparisons of hypoxic pocket properties between experimental conditions (e.g. KX vs awake) we used a linear mixed effects (LME) model approach to take into account the dependencies in our data (experimental conditions-mice-hypoxic pockets) and account for random effects (66). Statistical modelling routines for the LME models were written and run using the R package *nlme* in RStudio 2023.06.2 (Rstudio Team, 2016). *Post hoc* tests between groups were conducted by comparing

estimated marginal means with t-tests with a Tukey correction for multiple comparisons using the R package *emmeans*. One-sample t-tests were run using the R package *lmerTest* followed by correction for false discovery rate (alpha = 0.05) with Benjamini–Hochberg procedure. All other statistical comparisons were conducted using GraphPad (Prism 9).

For signal correlation between FluoSpheres and ΔpO_2 signals, Pearson’s correlation coefficient (r) values were transformed to (z) values. This is because r values are bounded between $[-1, 1]$, and the sampling distribution for highly correlated variables is highly skewed. Therefore, we converted the r value distribution to normal z value distribution using the *Fisher’s z* transformation:

$$z = (0.5) \ln \frac{1+r}{1-r} \text{ (Eq. 7)}$$

Data and statistical analysis for all figures are provided in Data S1.

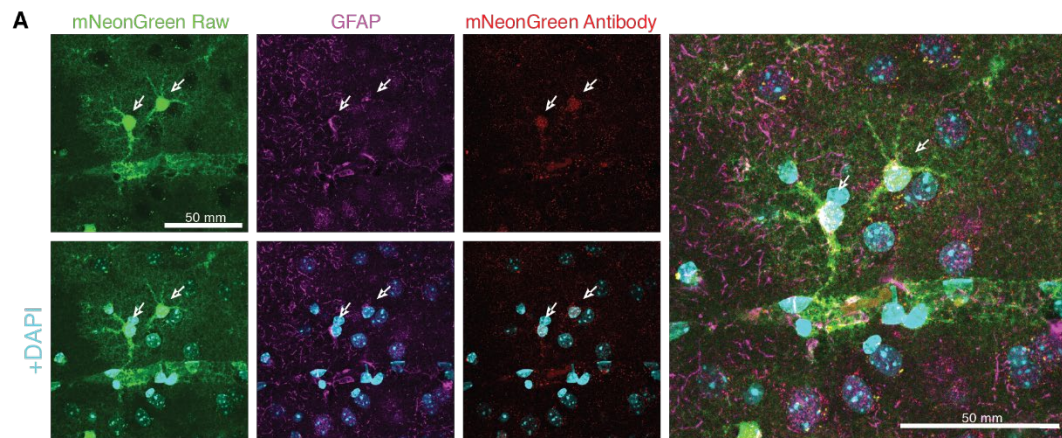


Fig. S1. Validation of cell specificity of GeNL expression. (A) Expression of GFAP-GeNL in cortical astrocytes. Overlay of mNeonGreen fluorescence (Green) with GFAP antibody staining (Purple) and mNeonGreen antibody (Red). Nuclei are labeled with DAPI (blue). Scale bars, 50 μ m.

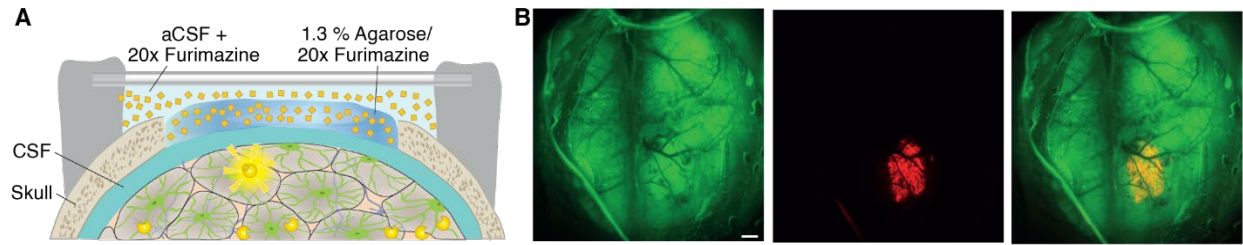


Fig. S2. Substrate administration and signal distribution. (A) Furimazine was embedded in 1.3% agarose (20x dilution) above the exposed cortex after dura removal. The agarose was covered with aCSF mixed with furimazine (20x diluted) and sealed with a cover glass to prevent auto oxidization of the substrate and to provide a reservoir of substrate for long-term recordings. (B) Bioluminescence intensity was limited to cranial window and area where dura has been removed. Green: Fluorescence of the sensor expressed in the whole brain after i.v. injection. Red: bioluminescence intensity. Scale bar, 500 μm .

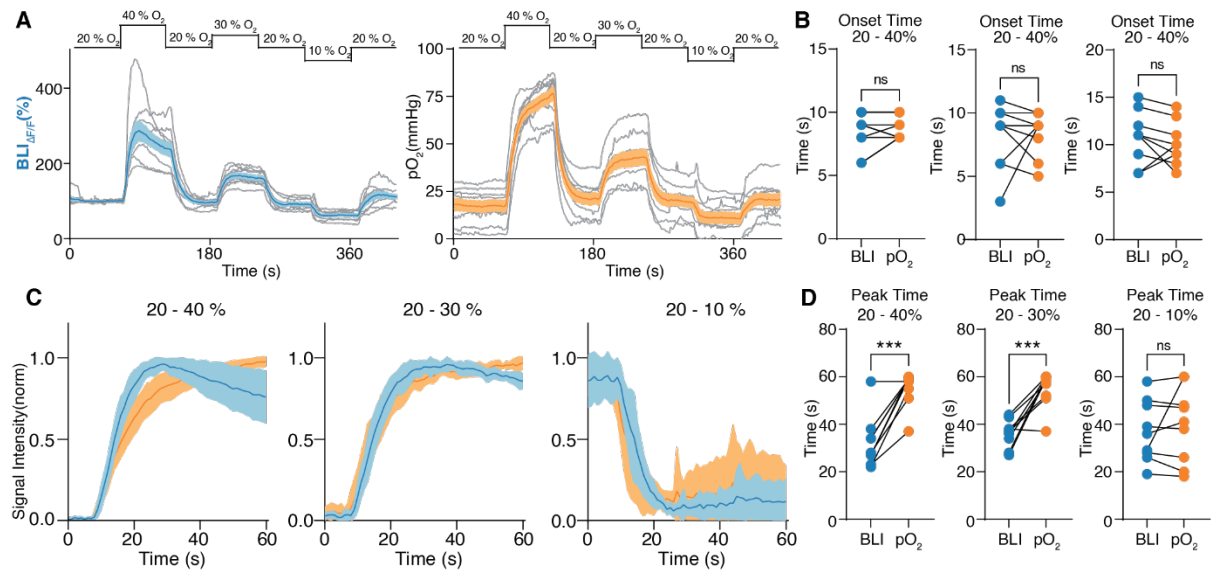


Fig. S3. Correlations of bioluminescence intensity and O₂-electrode recordings during oxygen calibration. (A) Single recordings from oxygen calibration. **(B)** Comparison of onset times between BLI and electrode recordings upon oxygen change. **(C)** Onset of BLI and electrode changes upon oxygen change normalized to the maximum value within a 60 s window. Shadow indicates standard deviation (SD). **(D)** Comparison of time until peak after oxygen change at different concentrations measured with BLI and electrode recordings. Paired t test. ***: P < 0.001. N = 9 trials from 6 mice.

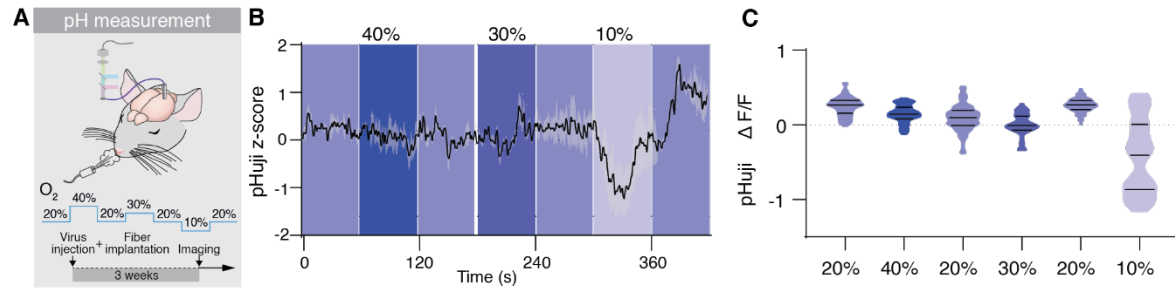


Fig. S4. Extracellular pH measurements during oxygen calibration show no relevant change. (A) Extracellular pH was measured in the cortex of KX anesthetized mice expressing the pHuji in the membrane of astrocytes facing the extracellular space. A fiber photometry probe was inserted, and oxygen concentration of the inhaled air was changed according to the protocol outlined. (B) Average trace of pH change represented as $\Delta F/F$ over time during O_2 manipulation in the tidal air. Shading indicates SEM. (C) Frequency distribution of pHuji $\Delta F/F$ at different O_2 levels. One-way RM ANOVA: $F_{5, 5492} = 417.7802$. $p < 0.0001$ main effect of group (no statistically significant differences from baseline=0). $N = 3$ mice.

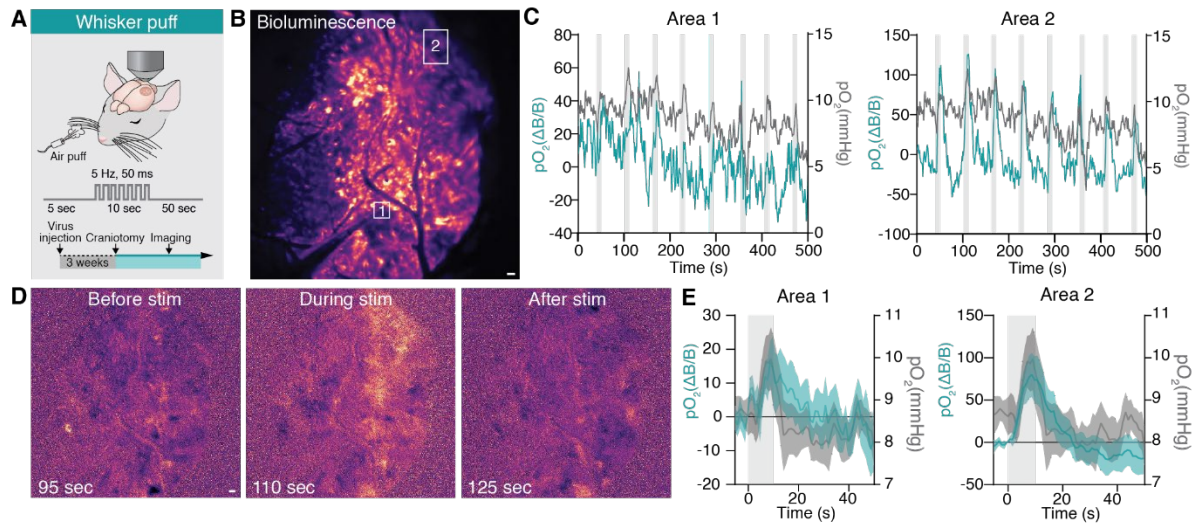


Fig. S5. Bioluminescence intensity follows O₂ electrode upon functional hyperemia. (A) Cerebral pO₂ was measured using BLI and an O₂-sensitive microelectrode in somatosensory cortex of KX anesthetized mice subjected to air-puff whisker stimulation at 5 Hz, 50 ms pulse duration, 20 psi for 10 s repeated 8 times every minute. (B) Average BLI distribution with indicated ROIs. (C) Time trace of bioluminescence intensity and O₂ electrode recordings from area 1 and 2 from B. (D) Representative images from single frames at indicated time points showing increase in BLI during whisker stimulation from B. Before, during, and after a series of air puffs. (E) Average trace of 8 repetitions of air puffs to the whiskers of ΔpO_2 measured with BLI and O₂-electrode from 2 areas indicated in D. Shading indicates SEM. Time point of whisker stimulation shown in light grey. Overall group effect $F_{2, 1176} = 0.0991$, $p = 0.90568$. Tukey posthocs: BLI Area 1 vs Electrode: $p = 0.9054$; BLI Area 2 vs Electrode: $p = 0.9948$. Scale bars, 100 μm .

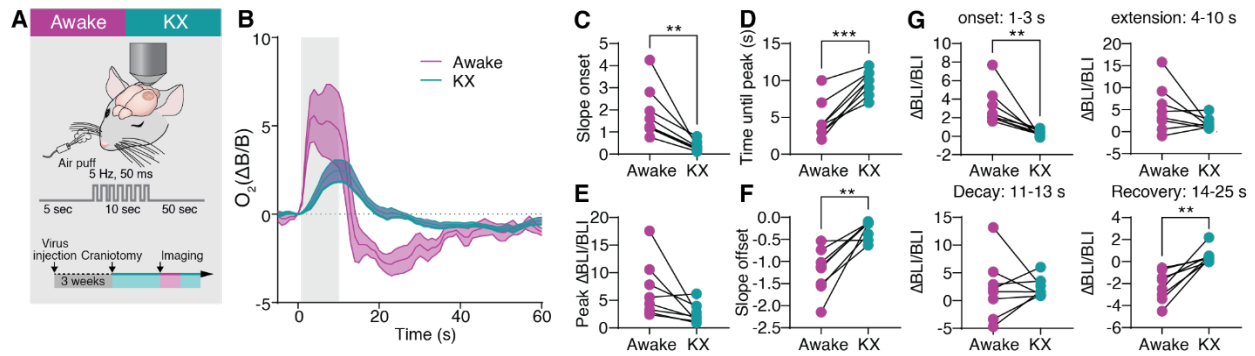


Fig. S6. Functional hyperemia is more prominent in awake mice compared to KX anesthetized mice. (A) Cerebral pO_2 during whisker stimulation was measured using bioluminescence intensity (BLI) in the cortex of KX anesthetized and awake mice subjected to air-puff whisker stimulation at 5 Hz, 50 ms pulse duration, 20 psi for 10 s repeated 8 times every minute. Mice were first measured awake followed by KX injection. (B) Average traces of change in BLI upon whisker stimulation over all trials. (C) Delay in slope onset between awake and KX mice. (D) Time until peak of BLI after stimulation onset. (E) Maximum BLI changes upon whisker stimulation. (F) Slope offset after whisker stimulation. (G) Average BLI from baseline at different time points. Upon onset (1 – 3 s), during extension time (4 – 10 s), in the decay phase after whisker puff (11 – 13 s), and in the recovery phase (14 – 25 s). Paired t test. $N = 8$ mice.

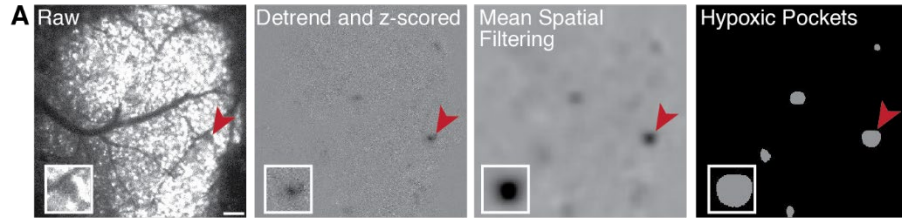


Fig. S7. Automatic detection pipeline for hypoxic pockets. (A) The raw image file is first detrended and hypoxic pockets are identified after mean spatial filtering. Scale bar: 100 μm .

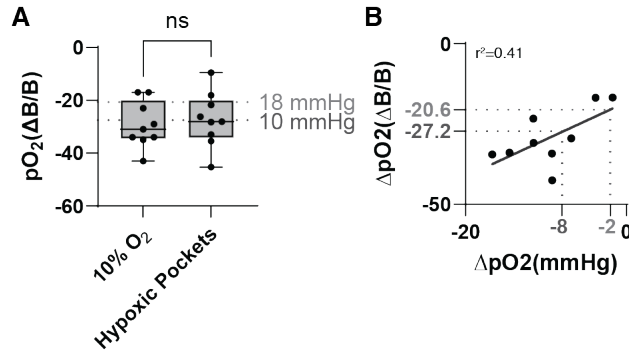


Fig. S8. Hypoxic pockets reach the hypoxic threshold. (A) Box and whisker plots showing BLI signal change [$pO_2(\Delta B/B)$] in response to reduction of inhaled oxygen concentration to 10% as well during hypoxic pocket events in KX anesthetized mice. On average, the change corresponds approximately to 10 mmHg tissue pO_2 . 18 mmHg is the previously determined hypoxic threshold. (B) Change in BLI and corresponding change in pO_2 recorded with the O_2 electrode in the same region upon changes in O_2 concentration of the inhalation air. This is effectively an aspect of already plotted data (Fig 2F) but focussing on hypoxia. Data points are fitted with a linear regression with an r^2 of 0.4. The x-axis corresponds to a decrease of tissue pO_2 from 20 mmHg (at 20% inhaled oxygen). A reduction of 2 mmHg equals 18 mmHg tissue pO_2 , and 8 mmHg equals 10 mmHg tissue pO_2 . Two-tailed unpaired t Test: $p = 0.67$. $N = 9$ trials from 6 mice (10% O_2) and $N = 9$ mice (Hypoxic Pockets).

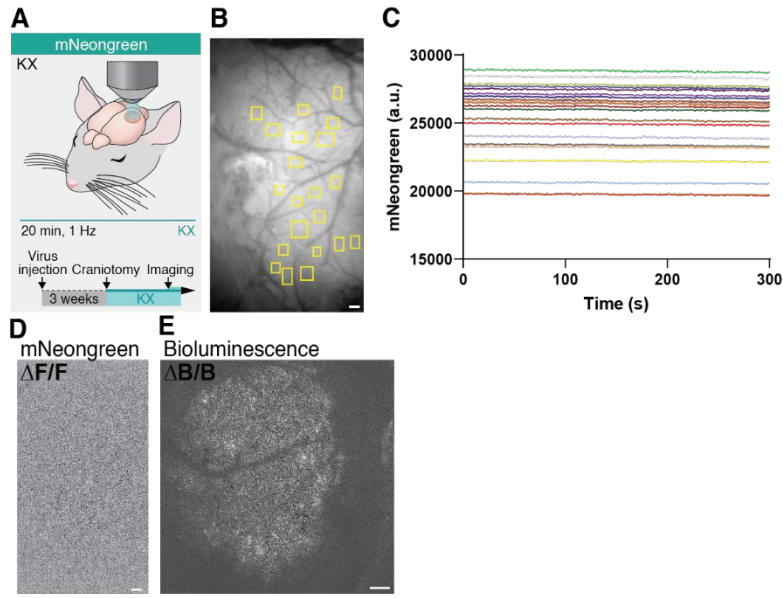


Fig. S9. mNeonGreen fluorescence is stable over time. (A) GeNL fluorescence was measured by excitation of mNeonGreen with a 490 nm LED in the cortex of KX anesthetized mice after acute craniotomy and furimazine administration. (B) Average projection of a 300 s long recording of mNeonGreen. Yellow squares indicate manually drawn ROIs. (C) mNeonGreen fluorescence over time. Each trace represents a ROI from B. (D) Average projection of the $\Delta F/F$ normalized recording B. (E) Average projection of the $\Delta B/B$ normalized bioluminescence image of a representative recording (from Fig. 2B). Brighter spots indicate changes from mean intensity. Scale bars, 100 μm .

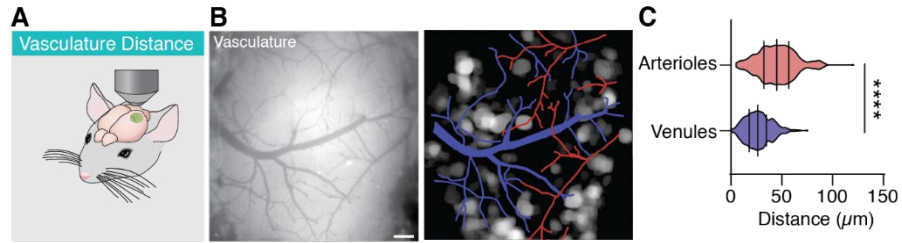


Fig. S10. Distance to vasculature. (A) Cerebral pO_2 was measured using bioluminescence intensity (BLI) in the cortex of awake mice and hypoxic pockets were identified. (B) Arterioles and venules were identified from white light images of the recording area, and distance to vasculature was measured from the centroid of the hypoxic pockets. (C) Frequency distribution of the distance of the centroid of a hypoxic pocket to the nearest arteriole and venule, respectively. One-way repeated measures ANOVA $F_{1, 3293} = 245.1$, $p < 0.0001$ main effect of group. $N = 8$ mice. Violin plots show median and quartiles. Scale bar, 100 μm .

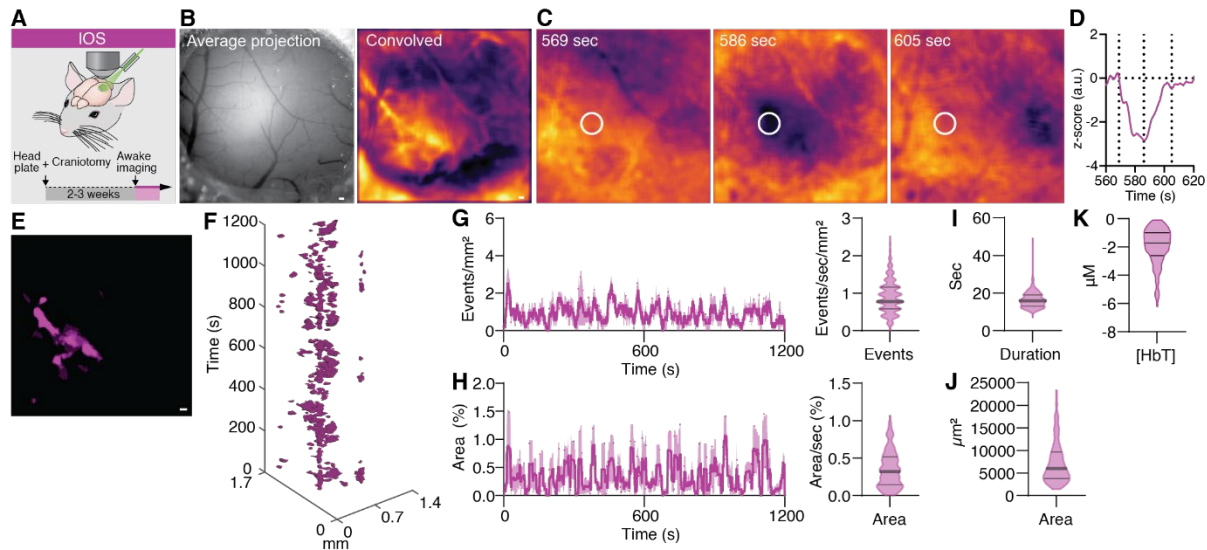


Fig. S11. Areas of low hemoglobin concentration. (A) Cerebral hemoglobin concentration ([HbT]) was imaged with intrinsic optical spectroscopy (IOS) at the isosbestic point for [HbT] in the somatosensory cortex through a cranial window in awake mice head restrained under a microscope for 20 minutes. (B) Left: Average projection of the reflection data of the mouse cortex illuminated with 525 nm LED. Right: Average projection after convolution of the raw reflection data. (C) Representative images recorded a 569, 586, and 605 s from B. (D) Time trace of hemoglobin concentration derived from the ROI marked in the convolved image series C. Dotted lines indicate timepoints from C. (E) Average projection of low flow areas from B. (F) Low flow areas detected from the IOS data in the form of regions of interest over time displayed in x-y-t 3D rendering. Lilac regions denote signal. (G) Average number of low flow areas per mm² detected per second. (H) Area covered by low flow areas per second. (I) Duration of low flow events. (J) Size of low flow areas. (K) Change in [HbT] during low flow events. *N* = 3 mice. Data represent mean ± SEM. SEM = standard error of the mean. Violin plots show median and quartiles. Scale bars: 100 μm.

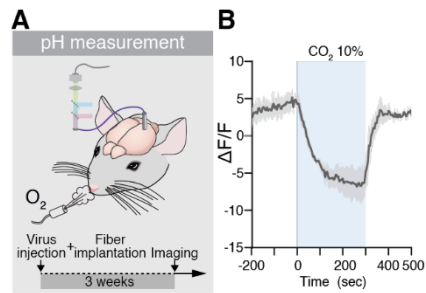


Fig. S12. Extracellular pH during hypercapnia. (A) Extracellular pH was measured in the cortex of KX anesthetized mice expressing pHuji in the membrane of astrocytes facing the extracellular space. A fiber photometry probe was inserted, and CO₂ concentration of the inhaled air was changed for five minutes during recording. (B) Time trace of the average change in pHuji fluorescence during hypercapnia (10% CO₂, blue shaded area). Data represents mean \pm SEM. SEM = standard error of the mean. $N = 3$ mice.

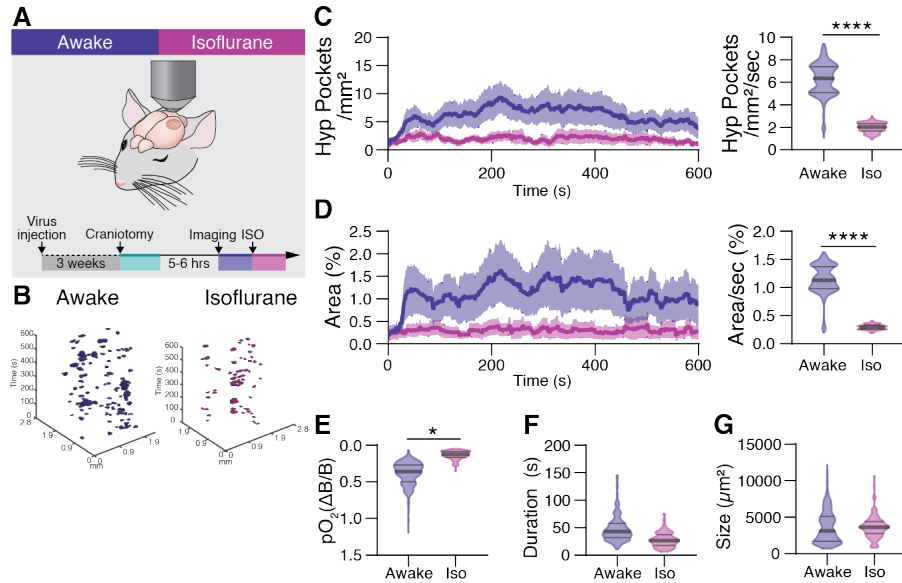


Fig. S13. Hypoxic pockets are suppressed by isoflurane-induced vasodilation. (A) Cerebral pO_2 was measured in awake head-fixed and isoflurane anesthetized mice, respectively, after acute craniotomy. First, mice were recorded for ten minutes awake followed by measurement under isoflurane anesthesia. (B) Hypoxic Pockets during quiet wakefulness (Left) and during isoflurane anesthesia (right) in the form of regions of interest over time displayed in a x-y-t 3D rendering. Blue regions denote signal from awake mice, lilac regions denote signal from isoflurane anesthetized mice. (C) Left: Average number of hypoxic pockets per mm^2 during transition from normoxia to hyperoxia. Shading indicates \pm SEM. Right: Number of hypoxic pockets per mm^2 per second. (D) Left: Average area covered by hypoxic pockets during transition from normoxia to hyperoxia. Shading indicates \pm SEM. Right: Area covered by pockets per second. (E) $pO_2(\Delta B/B)$ of hypoxic pockets. (F) Duration of hypoxic pockets. (G) Size of hypoxic pockets. $N = 7$ mice; Means \pm SEM are shown; SEM = standard error of the mean. Bars indicating Tukey's *post-hoc* tests between groups at their edges: *: $P < 0.05$, **: $P < 0.01$, ***: $P < 0.001$, ****: $P < 0.0001$.

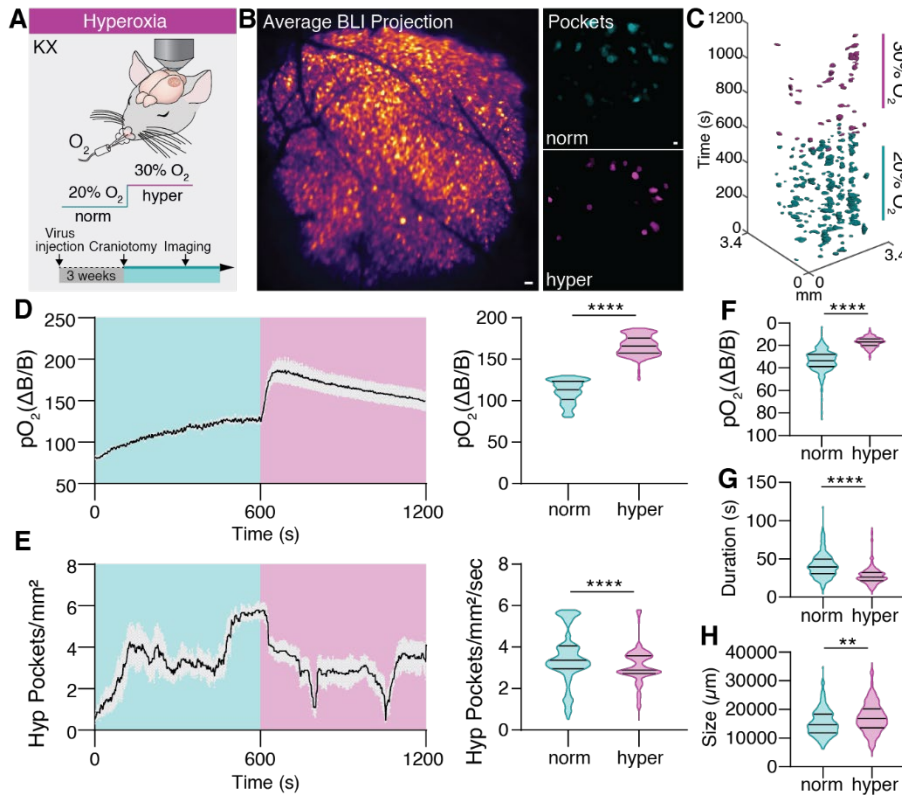


Fig. S14. High tissue oxygen diminishes hypoxic pockets. (A) Cerebral pO_2 was measured in KX anesthetized mice. Oxygen concentration in the inhaled air was increased from 20% (normoxic) to 30% (hyperoxic) for ten minutes after ten-minute baseline recording. (B) Left: Average bioluminescence intensity projection of a representative recording. Right: Projection of hypoxic pockets during period of normoxic (norm) and hyperoxic (hyper) conditions from the same recording. (C) Hypoxic pockets during the experiment in the form of regions of interest over time displayed in a x-y-t 3D rendering. Cyan regions denote signal during normoxia, lilac regions denote signal during hyperoxia. (D) Left: Average pO_2 traces during transition from normoxia to hyperoxia. Normalized to the first 600 s of the recording at normoxic conditions. Shading indicates \pm SEM. Right: pO_2 increases by 55% during hyperoxia. One-way Repeated measures ANOVA $F_{1, 2999} = 9529.9$, $p < 0.0001$ main effect of group. (E) Left: Average number of hypoxic pockets per mm^2 during transition from normoxia to hyperoxia. Shading indicates \pm SEM. Right: Number of hypoxic pockets per mm^2 per second decreases by 11%. One-way Repeated measures ANOVA $F_{1, 2999} = 31823.44$, $p < 0.0001$ main effect of group. (F) $pO_2(\Delta B/B)$ of hypoxic pockets. (G) Duration of hypoxic pockets. (H) Size of hypoxic pockets. In D and E data is shown as Mean \pm SEM. SEM = standard error of the mean. In D-H violin plots show median and quartiles. Bars indicating Tukey's *post-hoc* tests between groups at their edges: *: $P < 0.05$, **: $P < 0.01$, ***: $P < 0.001$, ****: $P < 0.0001$. Scale bars, 100 μm .; $N = 5$ mice.

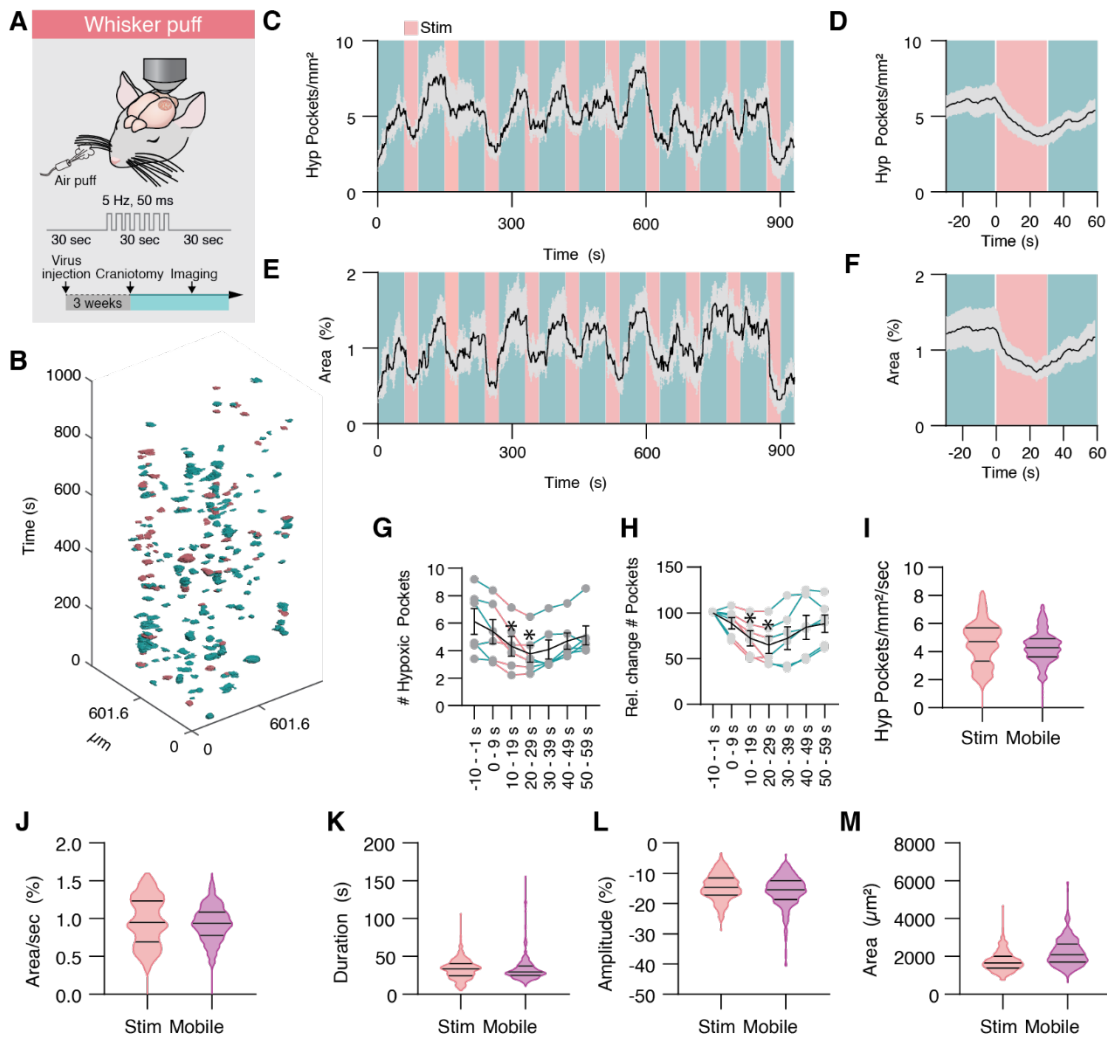


Fig. S15 Functional hyperemia reduces prevalence of hypoxic pockets. (A) Cerebral pO₂ during whisker stimulation was measured using bioluminescence intensity (BLI) in the cortex of KX anesthetized and awake mice subjected to air-puff whisker stimulation at 5 Hz, 50 ms pulse duration, 20 psi for 30 s repeated 10 times every 90 s. (B) Hypoxic pockets during the experiment in the form of regions of interest over time displayed in a x-y-t 3D rendering. Cyan regions denote signal during without stimulation, lilac regions denote signal during air puff administration. (C) Average number of hypoxic pockets per mm² during the experiment. Cyan indicates periods without stimulation. Lilac indicates periods of whisker stimulation. (D) Average traces of change in number of hypoxic pockets upon whisker stimulation over all trials. (E) Average area covered by hypoxic pockets during the experiment. (F) Average traces of change in area covered by hypoxic pockets upon whisker stimulation over all trials. (G) Change in number of hypoxic pockets in periods of 10 s. Each dot connected with a line represents a single recording. Black line with error bars (SEM) indicates average for all animals. (H) Change in relative number of hypoxic pockets in periods of 10 s normalized to the 10 s before stimulation onset. Each dot connected with a line represents a single recording. Black line with error bars (SEM) indicates average for all animals. (I) Frequency distribution of number of hypoxic pockets per second per mm² in mice exposed to functional stimulation and mobile mice. (J) Frequency distribution of area covered by hypoxic pockets per second in mice exposed to functional stimulation and mobile mice. (K)

Frequency distribution of duration of hypoxic pockets in mice exposed to functional stimulation and mobile mice. **(L)** Frequency distribution of relative pO₂ decrease of hypoxic pockets in mice exposed to functional stimulation and mobile mice. **(M)** Frequency distribution of size of hypoxic pockets in mice exposed to functional stimulation and mobile mice. Shading indicates \pm SEM. SEM = standard error of the mean. Violin plots show median and quartiles. Paired t test. *: P < 0.05. N = 6 mice.

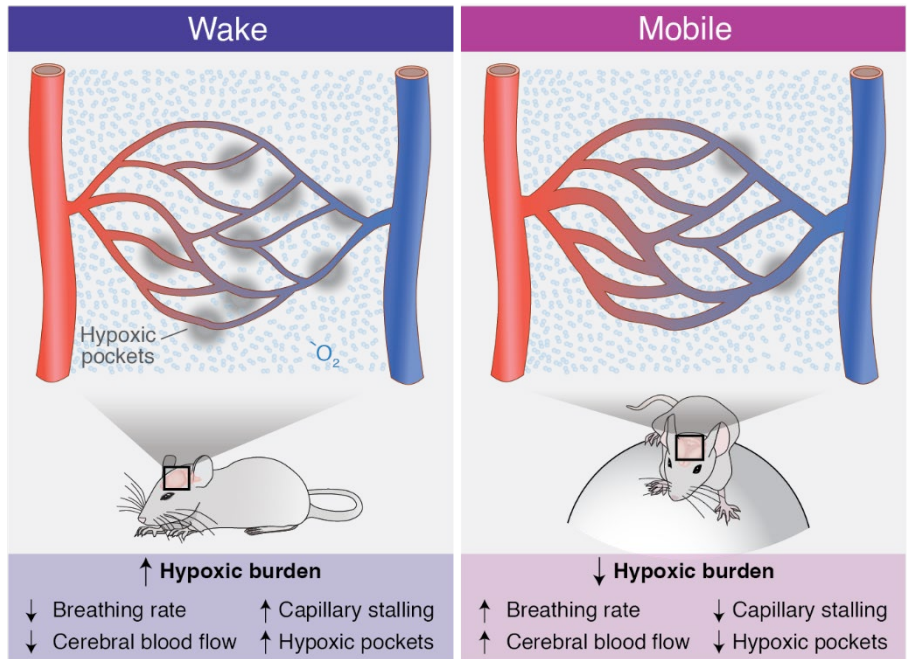


Fig. S16 Model explaining the effect of increased mobility on hypoxic pocket prevalence. (A) Left: The burden of hypoxic pockets is high during quiet wakefulness. Breathing rate and cerebral blood flow (CBF) variability are low, leading to an increase in capillary stalling and hypoxic pockets. Right: During mobile wakefulness, breathing rate (32) and CBF are increased, while capillary stalling and hypoxic pocket prevalence is reduced thus lowering the hypoxic burden.

Construct	Description	Company	Reference #
AAV5-GFAP(2.2)-GeNL-WPRE	Virus expressing GeNL under GFAP promoter	Vector Biolabs	171120#19
ssAAV-PHP.eB/2-hGFAP-GeNL-WPRE-bGHp(A)	Virus expressing GeNL under GFAP promoter in pHp.eB packaging for i.v. injection	Viral Vector Facility (VVF), Neuroscience Center Zürich	vHH1-PHP.eB
PHP.eB AAV2 GFAP-ILP.pHuji.PTD	Virus expressing extracellular pHuji under GFAP promoter in pH.eB. packaging for i.v. injection. GFAP-ILP.pHuji.PTD (meaning it has both Igk Leading Peptide and Pdgfr Transmembrane Domain). Outward facing pH sensor	Canadian Neurophotonics Platform Viral Vector Core	2884

Table S1.
List of AAV. Specifications of the virus injected.

Antigen	Immunogen	Manufacturer (CAT#)	Host & isotype	Dilution	Reference RRID#
mNeonGreen	mNeonGreen fluorescent protein derived from <i>Branchiostoma lanceolatum</i>	ChromoTek 32f6	Mouse/IgG2c	1:400	AB_2827566
GFAP	Glial fibrillary acidic protein (Bovine)	Agilent, Z0334	Rabbit/Ig fraction	1:500	AB_10013382
NeuN	The exact immunogen sequence used to generate this antibody is proprietary information	Abcam, ab177487	Rabbit/IgG	1:500	AB_2532109
Iba1	The exact immunogen sequence used to generate this antibody is proprietary information	Abcam, ab5076	Goat/IgG	1:500	AB_2224402

Table S2.

List of antibodies. Specifications of the antibodies used for immunohistochemistry.

Movie S1.

Change in bioluminescence intensity upon change in oxygen concentration of the inhaled air in a KX anesthetized mouse. Recorded at 1 Hz. Oxygen concentration was changed every 60 s in the following order: 20%, 40%, 20%, 30%, 20%, 10%, 20%.

Movie S2.

Change in bioluminescence intensity upon whisker stimulation in the barrel cortex of an awake mouse. Whiskers were stimulated with air puffs every 60 s beginning after 60 s for 10 s. Recorded at 1 Hz.

Movie S3.

20-minute-long recording of oxygen dynamics in the cortex of a KX anesthetized mouse. Recorded at 1 Hz.

Movie S4.

Montage of identified hypoxic pockets in a 20-minute-long recording of oxygen dynamics in the cortex of a KX anesthetized mouse. Left: raw bioluminescence intensity. Middle: Identified hypoxic pockets. Right: Overlay of hypoxic pockets and raw bioluminescence intensity. Recorded at 1 Hz.

References and Notes

1. S. S. Kety, "General metabolism of the brain *in vivo*" in *Metabolism of the Nervous System*, D. Richter, Ed. (Pergamon, 1957), pp. 221–237.
2. D. D. Clarke, L. Sokoloff, "Circulation and energy metabolism of the brain" in *Basic Neurochemistry: Molecular, Cellular and Medical Aspects*, G. J. Siegel, B. W. Agranoff, R. W. Albers, S. K. Fisher, M. D. Uhler, Eds. (Lippincott-Raven, ed. 6, 1999), pp. 637–689.
3. D. F. Rolfe, G. C. Brown, Cellular energy utilization and molecular origin of standard metabolic rate in mammals. *Physiol. Rev.* **77**, 731–758 (1997).
[doi:10.1152/physrev.1997.77.3.731](https://doi.org/10.1152/physrev.1997.77.3.731) [Medline](#)
4. T. Takano, G.-F. Tian, W. Peng, N. Lou, D. Lovatt, A. J. Hansen, K. A. Kasischke, M. Nedergaard, Cortical spreading depression causes and coincides with tissue hypoxia. *Nat. Neurosci.* **10**, 754–762 (2007). [doi:10.1038/nn1902](https://doi.org/10.1038/nn1902) [Medline](#)
5. B. Li, T. V. Esipova, I. Sencan, K. Kılıç, B. Fu, M. Desjardins, M. Moeini, S. Kura, M. A. Yaseen, F. Lesage, L. Østergaard, A. Devor, D. A. Boas, S. A. Vinogradov, S. Sakadžić, More homogeneous capillary flow and oxygenation in deeper cortical layers correlate with increased oxygen extraction. *eLife* **8**, e42299 (2019). [doi:10.7554/eLife.42299](https://doi.org/10.7554/eLife.42299) [Medline](#)
6. M. P. Hall, J. Unch, B. F. Binkowski, M. P. Valley, B. L. Butler, M. G. Wood, P. Otto, K. Zimmerman, G. Vidugiris, T. Machleidt, M. B. Robers, H. A. Benink, C. T. Eggers, M. R. Slater, P. L. Meisenheimer, D. H. Klaubert, F. Fan, L. P. Encell, K. V. Wood, Engineered luciferase reporter from a deep sea shrimp utilizing a novel imidazopyrazinone substrate. *ACS Chem. Biol.* **7**, 1848–1857 (2012).
[doi:10.1021/cb3002478](https://doi.org/10.1021/cb3002478) [Medline](#)
7. K. Suzuki, T. Kimura, H. Shinoda, G. Bai, M. J. Daniels, Y. Arai, M. Nakano, T. Nagai, Five colour variants of bright luminescent protein for real-time multicolour bioimaging. *Nat. Commun.* **7**, 13718 (2016). [doi:10.1038/ncomms13718](https://doi.org/10.1038/ncomms13718) [Medline](#)
8. D. Lambrechts, M. Roeffaers, K. Goossens, J. Hofkens, G. Vande Velde, T. Van de Putte, J. Schrooten, H. Van Oosterwyck, A causal relation between bioluminescence and oxygen to quantify the cell niche. *PLOS ONE* **9**, e97572 (2014).
[doi:10.1371/journal.pone.0097572](https://doi.org/10.1371/journal.pone.0097572) [Medline](#)
9. R. A. Pollock, R. T. Jackson, A. A. Clairmont, W. L. Nicholson, Carbon dioxide as an otic vasodilator. Otic blood flow as measured by the microsphere technique. *Arch. Otolaryngol.* **100**, 309–313 (1974). [doi:10.1001/archotol.1974.00780040319015](https://doi.org/10.1001/archotol.1974.00780040319015) [Medline](#)
10. J. Lee, T. Taira, P. Pihlaja, B. R. Ransom, K. Kaila, Effects of CO₂ on excitatory transmission apparently caused by changes in intracellular pH in the rat hippocampal slice. *Brain Res.* **706**, 210–216 (1996). [doi:10.1016/0006-8993\(95\)01214-1](https://doi.org/10.1016/0006-8993(95)01214-1) [Medline](#)
11. Y. Shen, M. Rosendale, R. E. Campbell, D. Perrais, pHuji, a pH-sensitive red fluorescent protein for imaging of exo- and endocytosis. *J. Cell Biol.* **207**, 419–432 (2014).
[doi:10.1083/jcb.201404107](https://doi.org/10.1083/jcb.201404107) [Medline](#)

12. S. Holstein-Rønso, Y. Gan, M. J. Giannetto, M. K. Rasmussen, B. Sigurdsson, F. R. M. Beinlich, L. Rose, V. Untiet, L. M. Hablitz, D. H. Kelley, M. Nedergaard, Glymphatic influx and clearance are accelerated by neurovascular coupling. *Nat. Neurosci.* **26**, 1042–1053 (2023). [doi:10.1038/s41593-023-01327-2](https://doi.org/10.1038/s41593-023-01327-2) [Medline](#)
13. D. G. Lyons, A. Parpaleix, M. Roche, S. Charpak, Mapping oxygen concentration in the awake mouse brain. *eLife* **5**, e12024 (2016). [doi:10.7554/eLife.12024](https://doi.org/10.7554/eLife.12024) [Medline](#)
14. A.-K. Aydin, C. Verdier, E. Chaigneau, S. Charpak, The oxygen initial dip in the brain of anesthetized and awake mice. *Proc. Natl. Acad. Sci. U.S.A.* **119**, e2200205119 (2022). [doi:10.1073/pnas.2200205119](https://doi.org/10.1073/pnas.2200205119) [Medline](#)
15. K. Xu, D. A. Boas, S. Sakadžić, J. C. LaManna, Brain tissue PO₂ measurement during normoxia and hypoxia using two-photon phosphorescence lifetime microscopy. *Adv. Exp. Med. Biol.* **977**, 149–153 (2017). [doi:10.1007/978-3-319-55231-6_20](https://doi.org/10.1007/978-3-319-55231-6_20) [Medline](#)
16. Y. Ma, M. A. Shaik, M. G. Kozberg, S. H. Kim, J. P. Portes, D. Timerman, E. M. C. Hillman, Resting-state hemodynamics are spatiotemporally coupled to synchronized and symmetric neural activity in excitatory neurons. *Proc. Natl. Acad. Sci. U.S.A.* **113**, E8463–E8471 (2016). [doi:10.1073/pnas.1525369113](https://doi.org/10.1073/pnas.1525369113) [Medline](#)
17. X. Zhu, Q. Huang, A. DiSpirito, T. Vu, Q. Rong, X. Peng, H. Sheng, X. Shen, Q. Zhou, L. Jiang, U. Hoffmann, J. Yao, Real-time whole-brain imaging of hemodynamics and oxygenation at micro-vessel resolution with ultrafast wide-field photoacoustic microscopy. *Light Sci. Appl.* **11**, 138 (2022). [doi:10.1038/s41377-022-00836-2](https://doi.org/10.1038/s41377-022-00836-2) [Medline](#)
18. A. R. Nippert, K. R. Biesecker, E. A. Newman, Mechanisms mediating functional hyperemia in the brain. *Neuroscientist* **24**, 73–83 (2018). [doi:10.1177/1073858417703033](https://doi.org/10.1177/1073858417703033) [Medline](#)
19. A. Villringer, A. Them, U. Lindauer, K. Einhüpl, U. Dirnagl, Capillary perfusion of the rat brain cortex. An in vivo confocal microscopy study. *Circ. Res.* **75**, 55–62 (1994). [doi:10.1161/01.RES.75.1.55](https://doi.org/10.1161/01.RES.75.1.55) [Medline](#)
20. D. A. Brodie, D. M. Woodbury, Acid-base changes in brain and blood of rats exposed to high concentrations of carbon dioxide. *Am. J. Physiol.* **192**, 91–94 (1958). [doi:10.1152/ajplegacy.1957.192.1.91](https://doi.org/10.1152/ajplegacy.1957.192.1.91) [Medline](#)
21. R. F. Cucchiara, R. A. Theye, J. D. Michenfelder, The effects of isoflurane on canine cerebral metabolism and blood flow. *Anesthesiology* **40**, 571–574 (1974). [doi:10.1097/00000542-197406000-00011](https://doi.org/10.1097/00000542-197406000-00011) [Medline](#)
22. S. Gelman, K. C. Fowler, L. R. Smith, Regional blood flow during isoflurane and halothane anesthesia. *Anesth. Analg.* **63**, 557–565 (1984). [doi:10.1213/00000539-198406000-00002](https://doi.org/10.1213/00000539-198406000-00002) [Medline](#)
23. L. A. Low, L. C. Bauer, B. A. Klaunberg, Comparing the effects of isoflurane and alpha chloralose upon mouse physiology. *PLOS ONE* **11**, e0154936 (2016). [doi:10.1371/journal.pone.0154936](https://doi.org/10.1371/journal.pone.0154936) [Medline](#)
24. D. Aksenov, J. E. Eassa, J. Lakhoo, A. Wyrwicz, R. A. Linsenmeier, Effect of isoflurane on brain tissue oxygen tension and cerebral autoregulation in rabbits. *Neurosci. Lett.* **524**, 116–118 (2012). [doi:10.1016/j.neulet.2012.07.019](https://doi.org/10.1016/j.neulet.2012.07.019) [Medline](#)

25. Ş. E. Erdener, J. Tang, A. Sajjadi, K. Kılıç, S. Kura, C. B. Schaffer, D. A. Boas, Spatio-temporal dynamics of cerebral capillary segments with stalling red blood cells. *J. Cereb. Blood Flow Metab.* **39**, 886–900 (2019). [doi:10.1177/0271678X17743877](https://doi.org/10.1177/0271678X17743877) [Medline](#)
26. C. Iadecola, The neurovascular unit coming of age: A journey through neurovascular coupling in health and disease. *Neuron* **96**, 17–42 (2017). [doi:10.1016/j.neuron.2017.07.030](https://doi.org/10.1016/j.neuron.2017.07.030) [Medline](#)
27. O. Bracko, J. C. Cruz Hernández, L. Park, N. Nishimura, C. B. Schaffer, Causes and consequences of baseline cerebral blood flow reductions in Alzheimer’s disease. *J. Cereb. Blood Flow Metab.* **41**, 1501–1516 (2021). [doi:10.1177/0271678X20982383](https://doi.org/10.1177/0271678X20982383) [Medline](#)
28. P. Reeson, B. Schager, M. Van Sprengel, C. E. Brown, Behavioral and neural activity-dependent recanalization of plugged capillaries in the brain of adult and aged mice. *Front. Cell. Neurosci.* **16**, 876746 (2022). [doi:10.3389/fncel.2022.876746](https://doi.org/10.3389/fncel.2022.876746) [Medline](#)
29. P. Reeson, K. Choi, C. E. Brown, VEGF signaling regulates the fate of obstructed capillaries in mouse cortex. *eLife* **7**, e33670 (2018). [doi:10.7554/eLife.33670](https://doi.org/10.7554/eLife.33670) [Medline](#)
30. D. S. Greenberg, A. R. Houweling, J. N. D. Kerr, Population imaging of ongoing neuronal activity in the visual cortex of awake rats. *Nat. Neurosci.* **11**, 749–751 (2008). [doi:10.1038/nn.2140](https://doi.org/10.1038/nn.2140) [Medline](#)
31. K. Masamoto, T. Obata, I. Kanno, Intracortical microcirculatory change induced by anesthesia in rat somatosensory cortex. *Adv. Exp. Med. Biol.* **662**, 57–61 (2010). [doi:10.1007/978-1-4419-1241-1_7](https://doi.org/10.1007/978-1-4419-1241-1_7) [Medline](#)
32. Q. Zhang, M. Roche, K. W. Gheres, E. Chaigneau, R. T. Kedarasetti, W. D. Haselden, S. Charpak, P. J. Drew, Cerebral oxygenation during locomotion is modulated by respiration. *Nat. Commun.* **10**, 5515 (2019). [doi:10.1038/s41467-019-13523-5](https://doi.org/10.1038/s41467-019-13523-5) [Medline](#)
33. V. Untiet, F. R. M. Beinlich, P. Kusk, N. Kang, A. Ladrón-de-Guevara, W. Song, C. Kjaerby, M. Andersen, N. Hauglund, Z. Bojarowska, B. Sigurdsson, S. Deng, H. Hirase, N. C. Petersen, A. Verkhratsky, M. Nedergaard, Astrocytic chloride is brain state dependent and modulates inhibitory neurotransmission in mice. *Nat. Commun.* **14**, 1871 (2023). [doi:10.1038/s41467-023-37433-9](https://doi.org/10.1038/s41467-023-37433-9) [Medline](#)
34. E. Chaigneau, M. Oheim, E. Audinat, S. Charpak, Two-photon imaging of capillary blood flow in olfactory bulb glomeruli. *Proc. Natl. Acad. Sci. U.S.A.* **100**, 13081–13086 (2003). [doi:10.1073/pnas.2133652100](https://doi.org/10.1073/pnas.2133652100) [Medline](#)
35. H. S. Wei, H. Kang, I. D. Rasheed, S. Zhou, N. Lou, A. Gershteyn, E. D. McConnell, Y. Wang, K. E. Richardson, A. F. Palmer, C. Xu, J. Wan, M. Nedergaard, Erythrocytes are oxygen-sensing regulators of the cerebral microcirculation. *Neuron* **91**, 851–862 (2016). [doi:10.1016/j.neuron.2016.07.016](https://doi.org/10.1016/j.neuron.2016.07.016) [Medline](#)
36. J. Grutzendler, M. Nedergaard, Cellular control of brain capillary blood flow: in vivo imaging veritas. *Trends Neurosci.* **42**, 528–536 (2019). [doi:10.1016/j.tins.2019.05.009](https://doi.org/10.1016/j.tins.2019.05.009) [Medline](#)

37. Y. Qi, M. Roper, Control of low flow regions in the cortical vasculature determines optimal arterio-venous ratios. *Proc. Natl. Acad. Sci. U.S.A.* **118**, e2021840118 (2021). [doi:10.1073/pnas.2021840118](https://doi.org/10.1073/pnas.2021840118) [Medline](#)
38. P. Blinder, P. S. Tsai, J. P. Kaufhold, P. M. Knutsen, H. Suhl, D. Kleinfeld, The cortical angiome: An interconnected vascular network with noncolumnar patterns of blood flow. *Nat. Neurosci.* **16**, 889–897 (2013). [doi:10.1038/nn.3426](https://doi.org/10.1038/nn.3426) [Medline](#)
39. K. Ogata, T. Kosaka, Structural and quantitative analysis of astrocytes in the mouse hippocampus. *Neuroscience* **113**, 221–233 (2002). [doi:10.1016/S0306-4522\(02\)00041-6](https://doi.org/10.1016/S0306-4522(02)00041-6) [Medline](#)
40. E. A. Bushong, M. E. Martone, Y. Z. Jones, M. H. Ellisman, Protoplasmic astrocytes in CA1 stratum radiatum occupy separate anatomical domains. *J. Neurosci.* **22**, 183–192 (2002). [doi:10.1523/JNEUROSCI.22-01-00183.2002](https://doi.org/10.1523/JNEUROSCI.22-01-00183.2002) [Medline](#)
41. K. A. Kasischke, E. M. Lambert, B. Panepento, A. Sun, H. A. Gelbard, R. W. Burgess, T. H. Foster, M. Nedergaard, Two-photon NADH imaging exposes boundaries of oxygen diffusion in cortical vascular supply regions. *J. Cereb. Blood Flow Metab.* **31**, 68–81 (2011). [doi:10.1038/jcbfm.2010.158](https://doi.org/10.1038/jcbfm.2010.158) [Medline](#)
42. A. Krogh, The number and distribution of capillaries in muscles with calculations of the oxygen pressure head necessary for supplying the tissue. *J. Physiol.* **52**, 409–415 (1919). [doi:10.1113/jphysiol.1919.sp001839](https://doi.org/10.1113/jphysiol.1919.sp001839) [Medline](#)
43. M. Moeini, X. Lu, P. K. Avti, R. Damseh, S. Bélanger, F. Picard, D. Boas, A. Kakkar, F. Lesage, Compromised microvascular oxygen delivery increases brain tissue vulnerability with age. *Sci. Rep.* **8**, 8219 (2018). [doi:10.1038/s41598-018-26543-w](https://doi.org/10.1038/s41598-018-26543-w) [Medline](#)
44. X. Lu, M. Moeini, B. Li, O. de Montgolfier, Y. Lu, S. Bélanger, É. Thorin, F. Lesage, Voluntary exercise increases brain tissue oxygenation and spatially homogenizes oxygen delivery in a mouse model of Alzheimer’s disease. *Neurobiol. Aging* **88**, 11–23 (2020). [doi:10.1016/j.neurobiolaging.2019.11.015](https://doi.org/10.1016/j.neurobiolaging.2019.11.015) [Medline](#)
45. Q. Zhang, K. W. Gheres, P. J. Drew, Origins of 1/f-like tissue oxygenation fluctuations in the murine cortex. *PLOS Biol.* **19**, e3001298 (2021). [doi:10.1371/journal.pbio.3001298](https://doi.org/10.1371/journal.pbio.3001298) [Medline](#)
46. C. Mathiesen, A. Brazhe, K. Thomsen, M. Lauritzen, Spontaneous calcium waves in Bergman glia increase with age and hypoxia and may reduce tissue oxygen. *J. Cereb. Blood Flow Metab.* **33**, 161–169 (2013). [doi:10.1038/jcbfm.2012.175](https://doi.org/10.1038/jcbfm.2012.175) [Medline](#)
47. S.-G. Kim, S. Ogawa, Biophysical and physiological origins of blood oxygenation level-dependent fMRI signals. *J. Cereb. Blood Flow Metab.* **32**, 1188–1206 (2012). [doi:10.1038/jcbfm.2012.23](https://doi.org/10.1038/jcbfm.2012.23) [Medline](#)
48. C. Iadecola, The pathobiology of vascular dementia. *Neuron* **80**, 844–866 (2013). [doi:10.1016/j.neuron.2013.10.008](https://doi.org/10.1016/j.neuron.2013.10.008) [Medline](#)
49. Y. Iturria-Medina, R. C. Sotero, P. J. Toussaint, J. M. Mateos-Pérez, A. C. Evans; Alzheimer’s Disease Neuroimaging Initiative, Early role of vascular dysregulation on late-onset Alzheimer’s disease based on multifactorial data-driven analysis. *Nat. Commun.* **7**, 11934 (2016). [doi:10.1038/ncomms11934](https://doi.org/10.1038/ncomms11934) [Medline](#)

50. J. C. de la Torre, Alzheimer disease as a vascular disorder: Nosological evidence. *Stroke* **33**, 1152–1162 (2002). [doi:10.1161/01.STR.0000014421.15948.67](https://doi.org/10.1161/01.STR.0000014421.15948.67) [Medline](#)
51. R. N. Kalaria, The role of cerebral ischemia in Alzheimer's disease. *Neurobiol. Aging* **21**, 321–330 (2000). [doi:10.1016/S0197-4580\(00\)00125-1](https://doi.org/10.1016/S0197-4580(00)00125-1) [Medline](#)
52. E. Farkas, P. G. Luiten, Cerebral microvascular pathology in aging and Alzheimer's disease. *Prog. Neurobiol.* **64**, 575–611 (2001). [doi:10.1016/S0301-0082\(00\)00068-X](https://doi.org/10.1016/S0301-0082(00)00068-X) [Medline](#)
53. W. Kuschinsky, O. B. Paulson, Capillary circulation in the brain. *Cerebrovasc. Brain Metab. Rev.* **4**, 261–286 (1992). [Medline](#)
54. J. C. Cruz Hernández, O. Bracko, C. J. Kersbergen, V. Muse, M. Haft-Javaherian, M. Berg, L. Park, L. K. Vinarcsik, I. Ivasyk, D. A. Rivera, Y. Kang, M. Cortes-Canteli, M. Peyrounette, V. Doyeux, A. Smith, J. Zhou, G. Otte, J. D. Beverly, E. Davenport, Y. Davit, C. P. Lin, S. Strickland, C. Iadecola, S. Lorthois, N. Nishimura, C. B. Schaffer, Neutrophil adhesion in brain capillaries reduces cortical blood flow and impairs memory function in Alzheimer's disease mouse models. *Nat. Neurosci.* **22**, 413–420 (2019). [doi:10.1038/s41593-018-0329-4](https://doi.org/10.1038/s41593-018-0329-4) [Medline](#)
55. Ş. E. Erdener, J. Tang, K. Kılıç, D. Postnov, J. T. Giblin, S. Kura, I. A. Chen, T. Vayisoğlu, S. Sakadžić, C. B. Schaffer, D. A. Boas, Dynamic capillary stalls in reperfused ischemic penumbra contribute to injury: A hyperacute role for neutrophils in persistent traffic jams. *J. Cereb. Blood Flow Metab.* **41**, 236–252 (2021). [doi:10.1177/0271678X20914179](https://doi.org/10.1177/0271678X20914179) [Medline](#)
56. A. Arias-Cavieres, M. A. Khuu, C. U. Nwakudu, J. E. Barnard, G. Dalgin, A. J. Garcia 3rd, A HIF1a-dependent pro-oxidant state disrupts synaptic plasticity and impairs spatial memory in response to intermittent hypoxia. *eNeuro* **7**, ENEURO.0024-20.2020 (2020). [doi:10.1523/ENEURO.0024-20.2020](https://doi.org/10.1523/ENEURO.0024-20.2020) [Medline](#)
57. S. Yan, W. Fu, C. Wang, J. Mao, B. Liu, L. Zou, C. Lv, Association between sedentary behavior and the risk of dementia: A systematic review and meta-analysis. *Transl. Psychiatry* **10**, 112 (2020). [doi:10.1038/s41398-020-0799-5](https://doi.org/10.1038/s41398-020-0799-5) [Medline](#)
58. D. A. Raichlen, D. H. Aslan, M. K. Sayre, P. K. Bharadwaj, M. Ally, S. Maltagliati, M. H. C. Lai, R. R. Wilcox, Y. C. Klimentidis, G. E. Alexander, Sedentary behavior and incident dementia among older adults. *JAMA* **330**, 934–940 (2023). [doi:10.1001/jama.2023.15231](https://doi.org/10.1001/jama.2023.15231) [Medline](#)
59. F. R. M. Beinlich, A. Asiminas, V. Untiet, Z. Bojarowska, V. Plá, B. Sigurdsson, V. Timmel, L. Gehrig, M. H. Graber, H. Hirase, M. Nedergaard, Oxygen Imaging of Hypoxic Pockets in the Mouse Cerebral Cortex [Data set], version 0.240215.0831, DANDI archive (2024); <https://doi.org/10.48324/dandi.000891/0.240215.0831>.
60. A. Asiminas, Temp2Spec/OxygenDynamics_Public: Science_2024, version Science_2024, Zenodo (2024); <https://doi.org/10.5281/zenodo.10629901>.
61. J. Schindelin, I. Arganda-Carreras, E. Frise, V. Kaynig, M. Longair, T. Pietzsch, S. Preibisch, C. Rueden, S. Saalfeld, B. Schmid, J.-Y. Tinevez, D. J. White, V. Hartenstein, K. Eliceiri, P. Tomancak, A. Cardona, Fiji: An open-source platform for biological-image analysis. *Nat. Methods* **9**, 676–682 (2012). [doi:10.1038/nmeth.2019](https://doi.org/10.1038/nmeth.2019) [Medline](#)

62. J. K. Gundersen, N. B. Ramsing, R. N. Glud, Predicting the signal of O₂ microsensors from physical dimensions, temperature, salinity, and O₂ concentration. *Limnol. Oceanogr.* **43**, 1932–1937 (1998). [doi:10.4319/lo.1998.43.8.1932](https://doi.org/10.4319/lo.1998.43.8.1932)
63. Y. Nasu, A. Aggarwal, G. N. T. Le, C. T. Vo, Y. Kambe, X. Wang, F. R. M. Beinlich, A. B. Lee, T. R. Ram, F. Wang, K. A. Gorzo, Y. Kamijo, M. Boisvert, S. Nishinami, G. Kawamura, T. Ozawa, H. Toda, G. R. Gordon, S. Ge, H. Hirase, M. Nedergaard, M.-E. Paquet, M. Drobizhev, K. Podgorski, R. E. Campbell, Lactate biosensors for spectrally and spatially multiplexed fluorescence imaging. *Nat. Commun.* **14**, 6598 (2023). [doi:10.1038/s41467-023-42230-5](https://doi.org/10.1038/s41467-023-42230-5) [Medline](#)
64. A. Edelstein, N. Amodaj, K. Hoover, R. Vale, N. Stuurman, Computer control of microscopes using μ Manager. *Curr. Protoc. Mol. Biol.* **92**, 14.20.1–14.20.17 (2010). [doi:10.1002/0471142727.mb1420s92](https://doi.org/10.1002/0471142727.mb1420s92) [Medline](#)
65. C. Kjaerby, M. Andersen, N. Hauglund, V. Untiet, C. Dall, B. Sigurdsson, F. Ding, J. Feng, Y. Li, P. Weikop, H. Hirase, M. Nedergaard, Memory-enhancing properties of sleep depend on the oscillatory amplitude of norepinephrine. *Nat. Neurosci.* **25**, 1059–1070 (2022). [doi:10.1038/s41593-022-01102-9](https://doi.org/10.1038/s41593-022-01102-9) [Medline](#)
66. D. A. Cantu, B. Wang, M. W. Gongwer, C. X. He, A. Goel, A. Suresh, N. Kourdougli, E. D. Arroyo, W. Zeiger, C. Portera-Cailliau, EZcalcium: Open-Source toolbox for analysis of calcium imaging data. *Front. Neural Circuits* **14**, 25 (2020). [doi:10.3389/fncir.2020.00025](https://doi.org/10.3389/fncir.2020.00025) [Medline](#)
67. K. L. Turner, K. W. Gheres, E. A. Proctor, P. J. Drew, Neurovascular coupling and bilateral connectivity during NREM and REM sleep. *eLife* **9**, e62071 (2020). [doi:10.7554/eLife.62071](https://doi.org/10.7554/eLife.62071) [Medline](#)
68. Z. Yu, M. Guindani, S. F. Grieco, L. Chen, T. C. Holmes, X. Xu, Beyond t test and ANOVA: Applications of mixed-effects models for more rigorous statistical analysis in neuroscience research. *Neuron* **110**, 21–35 (2022). [doi:10.1016/j.neuron.2021.10.030](https://doi.org/10.1016/j.neuron.2021.10.030) [Medline](#)